On the Use of Nonlinear Boundary-Value Problems to Estimate the Cloud-Formation Potential of Aerosol Particles[*]

Mehdi Saghafi[†], Harry Dankowicz[†], and Matthew West[†]

Abstract. This paper investigates the transient growth of aerosol particles in a humid environment. It seeks to explore the dependence of the fraction of droplet-forming particles on statistical properties of the distribution of dry particle diameters, as well as on the rate of temperature decay associated with vertical motion through the atmosphere. Low-dimensional, autonomous models are investigated using basic tools of dynamical systems analysis that establish the parameter-dependent existence and stability of families of equilibrium distributions of wet particle diameters. In the fully nonautonomous case, an original heuristic parameterization of the fraction of droplet-forming particles is derived in terms of a scalar, nonlinear boundary-value problem. To address the failure of the heuristic parameterization to account for the potential of a dynamic reversal of growth following an initial increase in particle diameter, a finely resolved, high-dimensional boundary-value formulation for the aerosol dynamics is investigated using methods of numerical continuation. In order to reduce the computational complexity of the numerical scheme, an adaptive asynchronous discretization algorithm is developed in which the state variables are partitioned across distinct temporal meshes. Results obtained from the proposed numerical scheme are compared with the estimated fractions of droplet-forming particles based on available approximate criteria in the literature and demonstrate relative errors as large as 20%. The analysis further uncovers a hitherto-unknown linear relationship between the arithmetic expectation and variance of a log-normal size distribution of dry diameters for fixed fractions of droplet-forming particles.

Key words. aerosol particles, cloud condensation nuclei, particle activation, kinetic limitation, bifurcation analysis, boundary-value problems, slow-fast dynamics, asynchronous collocation

AMS subject classifications. 34C23, 37N10, 65L04, 65L09, 65L10, 65L60, 70K70

DOI. 10.1137/140987821

1. Introduction. The presence of clouds in the atmosphere may drastically influence the albedo of the earth to solar radiation by degrading the normal radiative heat exchange between the earth and the atmosphere. For this reason, the study of the formation of clouds is of great importance in the study of long-term climate change. Aerosol particles, originating from a variety of natural and anthropogenic sources [18] including sea salt and sulfur emissions, are known sinks for significant condensation of atmospheric water vapor. The role of aerosol particles as cloud condensation nuclei has, therefore, been the subject of extensive study [3, 4, 13, 33, 38]. Indeed, the influence of anthropogenic aerosol particles on the optical properties of clouds remains a major source of uncertainty in climate simulations. Collectively, all mechanisms through which climate is affected by the influence of aerosols on the number

[†]Department of Mechanical Science and Engineering, University of Illinois at Urbana-Champaign, Urbana, IL 61801 (msagha2@illinois.edu, danko@illinois.edu, mwest@illinois.edu).

concentration of droplets are referred to as the *aerosol indirect effect on climate* [26, 27, 28, 36].

For an adiabatic control volume, the supply of water vapor is limited, and aerosol particles compete for its absorption. For each particle, growth is maintained as long as the ambient relative humidity exceeds a particle-size-dependent lower bound. Particles that absorb sufficient amounts of atmospheric water vapor to form cloud droplets are said to be *activated*. Those that never grow appreciably, or experience initial rapid growth followed by a reversal back to a nearly dry state, are said to be *nonactivated*. For the purposes of climate simulations, the fraction of activated particles is of great practical importance, and techniques that yield accurate estimates of this fraction at low cost are highly desirable.

A brute-force method for predicting the fraction of activated particles is based on forward numerical simulation of the (integro-)differential equations governing the ambient relative humidity and the wet diameters for a population of particles of some known distribution of dry diameters. It is straightforward, but costly, to systematically explore the sensitivity of the estimated fraction of activated particles to the physical properties of the particles, the statistical distribution of dry diameters, and the ambient environment.

An alternative, heuristic approach to estimating the fraction of activated particles is based on simple algebraic threshold criteria applied to the distribution of dry aerosol diameters. Such criteria are commonly expressed in terms of the predicted maximal value of the relative humidity, for given initial conditions, and each particle's critical saturation ratio, evaluated for the ambient temperature obtained at the moment that the maximum in the relative humidity is reached [1, 2, 17, 23, 32] (for a review see [16]). In a typical approach, quasi-static approximations are used to parameterize the time-dependence of the relative humidity on key model parameters in order to arrive at algebraic relationships between physical parameters and the unknown fraction of activated particles.

The simplifying assumptions employed in the heuristic analysis fail to account for dynamic effects associated with the relative rates of growth of the particle diameters and the ambient relative humidity. In particular, they do not recognize circumstances in which a reversal in the growth of individual particle diameters follows an initial phase of rapid growth. Particles that experience such reversal are said to be *kinetically limited* [12, 31]. Failure to account for the effects of kinetic limitation therefore leads to an overestimation of the fraction of activated particles, with an error potentially of the same order of magnitude as the predicted fraction.

The objective of this paper is to further explore the growth dynamics of a population of aerosol particles in an adiabatic control volume with a given supply of water vapor in order to associate the fraction of activated and kinetically limited particles with statistical properties of the distribution of dry particle diameters. The analysis is framed in the context of cloud formation when the control volume experiences a linear drop in temperature (and an expansion in volume under conditions of constant pressure) associated with a vertical motion through the atmosphere (cf. [11] and [29], but see also [41, section 17.3.2]). The paper applies tools of basic bifurcation analysis to low-dimensional approximations of the coupled system dynamics in the case of constant-temperature operating conditions (for which the models are autonomous) to build basic intuition into the key features governing activation and kinetic limitation. For the case of nonautonomous operating conditions associated with known temperature variations, it proceeds to explore an original derivation of an implicit, physical parameterization of the fraction of activated particles (ignoring the effects of kinetic

limitation) in terms of a nonlinear, scalar boundary-value problem. Finally, the effects of kinetic limitation are investigated numerically for fixed fractions of activated particles using methods of numerical continuation applied to a high-dimensional nonlinear boundary-value problem.

The analysis in this paper makes original contributions to the understanding of both the autonomous and nonautonomous dynamics, with particular emphasis on a critical evaluation of the errors incurred in a heuristic parameterization of the fraction of activated particles. The derivation of the scalar-valued boundary-value formulation proceeds in analogy with work by Pinsky et al. [34, 35], albeit applied to a different system of governing equations, with greater attention paid to the nonuniqueness of solutions in a neighborhood of a manifold along which a key vector field is nondifferentiable. The numerical analysis of the high-dimensional boundary-value problem uncovers a linear relationship between the arithmetic expectation and variance of a log-normal size density function for fixed fractions of activated particles. It predicts relative errors due to overestimation, as would have been arrived at through the application of simple activation threshold criteria, as large as 20%.

A key computational advance is the development of asynchronous discretization schemes in order to enable efficient numerical study of the high-dimensional boundary-value problem within available resources. Here, the simultaneous analysis of the transient dynamics of thousands of states, whose time-dependence exhibits dramatically different characteristic time scales over different phases of evolution, calls for mesh discretization schemes that are adapted to the solution properties and possibly distinct across groups of state variables. Such asynchronous discretization schemes have been used in finite-element problems (where they are called *subcycling*), in which different time steps are used for different spatial domains to overcome the efficiency issue in large-scale problems with stiff elements [8, 9, 10, 20]. Similar ideas of partitioning to ensure an efficient and stable solution strategy in forward simulation of systems of ordinary differential equations are discussed in [15, 19, 40] (see [14, 24, 25] for recent work) and more generally in [5].

The remainder of this paper is organized as follows. In section 2, we describe the coupled (integro-)differential equations that govern the growth dynamics of a population of initially dry aerosol particles of some given size density under assumptions of adiabatic evolution of a given control volume and a spatially homogenized particle concentration. We explore the basic bifurcation characteristics of low-dimensional, autonomous models of the growth dynamics and develop a heuristic parameterization of the fraction of activated particles for a given temperature profile using a scalar, nonlinear, nonautonomous boundary-value problem. The effects of kinetic limitation and the need for a finely resolved, high-dimensional boundary-value formulation are investigated in section 3. This includes a discussion of the computational scheme employed in determining a relationship between the statistical properties of the particle size distribution for fixed fractions of activated particles. The section further reports on numerical predictions of the fraction of kinetically limited particles under variations in selected model parameters.

The technical details involved in the development of an adaptive, asynchronous collocation scheme for a nonlinear boundary-value problem are described in depth in an appendix to the main text. This includes a heuristic algorithm for determining optimal partitions among the state variables over distinct segments of the transient dynamics, as well as a preliminary

numerical analysis of rates of convergence in the context of a typical slow-fast system. A second appendix includes a brief derivation of the properties of nontrivial solutions based at points of nondifferentiability of a scalar vector field, previously found using numerical simulations by Pinsky et al. [34, 35].

2. Model description. The equations governing time-dependent variations in the size of cloud-condensation nuclei may be derived by considering a control volume containing a given concentration of aerosol particles [41, Chapter 17]. Such a model assumes that the effects of emissions, dilution, and coagulation between particles are negligible and that the condensation/evaporation of water onto/from individual particles is coupled to the availability of water vapor represented by the relative humidity. In particular, it assumes adiabatic evolution of the control volume with a fixed total water content. In addition, each particle is assumed to be composed of "dry" material and water, where the composition of the dry material is identical for all particles. Each particle has an individual fixed amount of dry material, specified by the diameter D_{dry} of the sphere containing just the particle's dry material, and a time-varying individual amount of water, which leads to the wet or total diameter D of the sphere containing all material (dry and water) in the particle.

2.1. A finite-dimensional discretization. Consider a continuum limit, in which the population of aerosol particles within the adiabtic control volume may be described in terms of a spatially homogenized number concentration per unit volume c and a density function $f : \mathbb{R}_+ \mapsto [0, 1]$, such that the number concentration per unit volume of particles of dry diameter in the interval $[D_{\text{dry}}, D_{\text{dry}} + \text{d}D_{\text{dry}}]$, at any location within the control volume, equals $cf(D_{\text{dry}}) \, \text{d}D_{\text{dry}}$. As a special case of significance in the analysis below, suppose, for example, that the size distribution is given by the log-normal density

$$(2.1) \qquad f_{\text{l.n.}} : D_{\text{dry}} \mapsto \frac{1}{D_{\text{dry}}\sqrt{2\pi}\sigma} e^{-\frac{(\ln D_{\text{dry}} - \mu)^2}{2\sigma^2}}$$

and the corresponding cumulative distribution

$$(2.2) \qquad F_{\text{l.n.}}(D_{\text{dry}}) := \int_0^{D_{\text{dry}}} f_{\text{l.n.}}(\eta) \, \text{d}\eta = \frac{1}{2}\left(1 - \text{erf}\left(\frac{\mu - \ln D_{\text{dry}}}{\sqrt{2}\sigma}\right)\right),$$

with (arithmetic) expected value $E_{\text{l.n.}} = e^{\mu + \sigma^2/2}$ and variance $V_{\text{l.n.}} = E_{\text{l.n.}}^2(e^{\sigma^2} - 1)$. It follows that the fraction of particles of dry diameter greater than some critical value D_{dry}^* is given by

$$(2.3) \qquad p := 1 - F_{\text{l.n.}}(D_{\text{dry}}^*) = \frac{1}{2}\left(1 + \text{erf}\left(\frac{\mu - \ln D_{\text{dry}}^*}{\sqrt{2}\sigma}\right)\right).$$

Let $D(D_{\text{dry}}, t)$ denote the wet diameter at time t of an aerosol particle with dry diameter D_{dry}. Denote the dimensionless *environmental saturation ratio* (i.e., the relative humidity), the *ambient temperature* (in units of K), and the *saturation vapor pressure* (in units of Pa) by S, T, and P, respectively, such that $S = S_{\text{dry}}$, $T = T_{\text{dry}}$, and $P = P_{\text{dry}}$ when the dry aerosol particles are deposited in the control volume. The dependence of the relative humidity on

Table 1
Numerical values of the model parameters.

Parameter	Symbol	Value	Unit
Density of water	ρ_w	1000	$\mathrm{kg\,m^{-3}}$
Aerosol number concentration	c_dry	10^{10}	$\mathrm{m^{-3}}$
Molecular weight of water	M_w	18×10^{-3}	$\mathrm{kg\,mol^{-1}}$
Universal gas constant	R	8.314472	$\mathrm{J\,mol^{-1}\,K^{-1}}$
Surface tension of water	σ_w	0.073	$\mathrm{J\,m^{-2}}$
Initial temperature	T_dry	290	K
Hygroscopicity	κ	0.5	

variations in the wet diameters of the aerosol particles within the control volume, under conditions of constant pressure, is then governed by the parameter

$$(2.4) \qquad \gamma := \frac{\pi \rho_w c_\mathrm{dry} R T_\mathrm{dry}}{6 M_w},$$

where c_dry is the value of c at the moment the dry aerosol particles are deposited in the control volume, ρ_w is the water density, M_w is the molecular weight of water, and R is the universal gas constant. Throughout this paper these quantities have the numerical values shown in Table 1. These parameters describe an initial aerosol number concentration and temperature that are representative of warm-cloud-formation atmospheric conditions [41], and we choose a moderate particle hygroscopicity of $\kappa = 0.5$, corresponding to mixed salt/organic particles in the middle of the typical atmospheric range of $0.1 < \kappa < 0.9$ [33]. Specifically, from a mass balance relation [41, section 10.2], it follows that

$$(2.5) \qquad \frac{d}{dt}(PS) = -3\gamma \int_0^\infty D(D_\mathrm{dry}, t)^2 \frac{\partial}{\partial t} D(D_\mathrm{dry}, t)\, f(D_\mathrm{dry})\, dD_\mathrm{dry}.$$

We arrive at a finite-dimensional model by substituting an equally weighted, discrete approximant for the density function in terms of a sample of N_p particles, and replacing (2.5) by the corresponding Riemann sum to yield

$$(2.6) \qquad \frac{d}{dt}(PS) = -\frac{3\gamma}{N_\mathrm{p}} \sum_{i=1}^{N_\mathrm{p}} D_i^2 \dot{D}_i.$$

Here, D_i denotes the wet diameter of an equivalent aerosol particle whose dry diameter $D_{i,\mathrm{dry}}$ is defined implicitly in terms of the corresponding cumulative distribution by

$$(2.7) \qquad F(D_{i,\mathrm{dry}}) = \xi + \frac{1 - 2\xi}{N_\mathrm{p} - 1}(i - 1)$$

for some $\xi > 0$.

2.2. Autonomous dynamics. In the autonomous case, the ambient temperature and saturation vapor pressure are both constant. In this case, variations in D beyond the dry diameter D_dry are governed by a differential equation of the form [41, section 17.4]

$$(2.8) \qquad \dot{D} = r(D)(S - q(D; D_\mathrm{dry})),$$

where

$$(2.9) \qquad r : D \mapsto \frac{\alpha_0}{D + \alpha_1}$$

and

$$(2.10) \qquad q : (D; D_{\mathrm{dry}}) \mapsto \frac{D^3 - D_{\mathrm{dry}}^3}{D^3 + (\kappa - 1) D_{\mathrm{dry}}^3} e^{\beta/D}$$

for some positive constants α_0, α_1, β, and the aerosol *hygroscopicity* (i.e., capacity to absorb water vapor) κ. From Petters and Kreidenweis [33], we find that typical aerosol species correspond to nonnegative values of κ limited from above by around 1.4. In the analysis below, we assume that this bound holds throughout.

2.2.1. Köhler curves. The following initial characterizations of the function $q(D; D_{\mathrm{dry}})$ provide a foundation for the analysis of the aerosol size dynamics.

Lemma 2.1. *The function $q(D; D_{\mathrm{dry}})$ has a unique local maximum for some critical diameter greater than D_{dry}.*

Proof. The function $q(D; D_{\mathrm{dry}})$ equals 0 for $D = D_{\mathrm{dry}}$ and converges to 1 from above as $D \to \infty$. Indeed, the sign of the partial derivative $\partial_D q(D; D_{\mathrm{dry}})$ equals that of the polynomial

$$(2.11) \qquad p(D; D_{\mathrm{dry}}) := 3D^4 D_{\mathrm{dry}}^3 \kappa - \left(D^3 - D_{\mathrm{dry}}^3\right)\left(D^3 - D_{\mathrm{dry}}^3 + D_{\mathrm{dry}}^3 \kappa\right)\beta,$$

which is positive when $D = D_{\mathrm{dry}}$ and negative for sufficiently large D. It follows that there exists at least one local maximum for some critical diameter greater than D_{dry}. The total number of local extrema of $q(D; D_{\mathrm{dry}})$ for $D > D_{\mathrm{dry}}$ equals the number of roots of the polynomial $p(D_{\mathrm{dry}} + \delta; D_{\mathrm{dry}})$ with $\delta > 0$. By Descartes's rule, an upper bound for this number is given by the number of sign changes in the sequence

$$(2.12) \qquad 1,\ 4 - \tilde{\beta},\ 6\kappa - \tilde{\beta}(\kappa + 3),\ 12\kappa - \tilde{\beta}(18 + \kappa),\ \kappa - 5\tilde{\beta},\ -1$$

for $\tilde{\beta} > 0$. For $\kappa < 1.4$, this number equals 1, and the claim follows. ∎

For an alternative proof of this result, we refer the reader to the discussion following equation (8) in [37]. The proof above is a precursor for the results below.

Corollary 2.2. *The maximum of $q(D; D_{\mathrm{dry}})$ is greater than 1.*

We denote the value of D at the local maximum of $q(D; D_{\mathrm{dry}})$ by D_{crit} and refer to the value $q(D_{\mathrm{crit}}; D_{\mathrm{dry}})$ as the *critical saturation ratio* associated with the dry diameter D_{dry}. Since this value is greater than 1, the excess $q(D_{\mathrm{crit}}; D_{\mathrm{dry}}) - 1$ is called the *critical supersaturation*, and the diameter D_{crit} is referred to as the corresponding *supersaturation point*. The graph of $q(D; D_{\mathrm{dry}})$ as a function of D is known as a *Köhler curve*. Several such curves are shown in Figure 1.

Lemma 2.3. *No two Köhler curves intersect.*

Proof. The claim follows from the observation that

$$(2.13) \qquad \partial_{D_{\mathrm{dry}}} q(D; D_{\mathrm{dry}}) = -\frac{3D^3 D_{\mathrm{dry}}^2 \kappa}{\left(D^3 + D_{\mathrm{dry}}^3(\kappa - 1)\right)^2} e^{\beta/D}$$
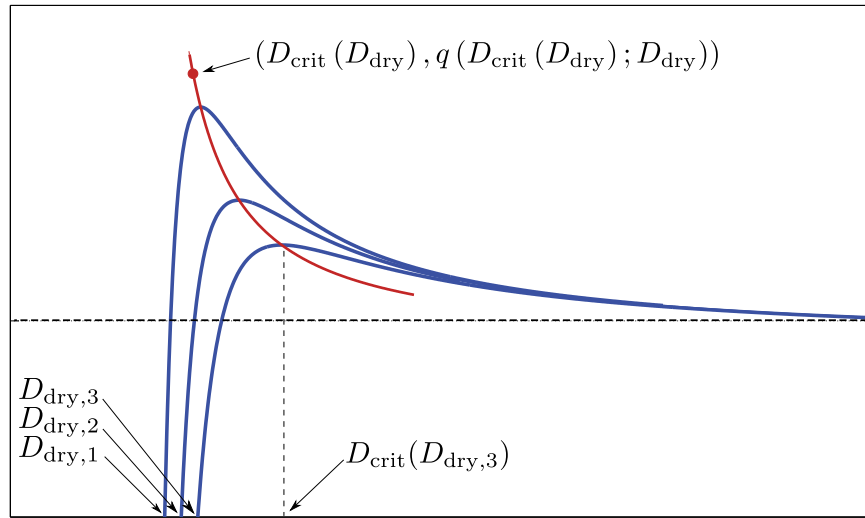
Figure 1. *Köhler curves for different dry diameters. The red curve shows the loci of global maxima corresponding to pairs of supersaturation points and critical saturation ratios.*

is everywhere negative. ■

Corollary 2.4. *The critical supersaturation is a decreasing function of* D_{dry}.

Further information about the shape of individual Köhler curves may be gleaned from the following lemma.

Lemma 2.5. *Suppose that* $q(D_1; D_{\mathrm{dry}}) = q(D_2; D_{\mathrm{dry}})$ *for* D_1 *and* D_2 *to the left and right, respectively, of* D_{crit}. *Then the slope of the graph of* $q(D; D_{\mathrm{dry}})$ *at* $D = D_1$ *is greater than the negative of the slope at* $D = D_2$.

Proof. For $\kappa < 1.4$, an analysis based on Descartes's rule shows that there is a unique inflection point along every Köhler curve and that this occurs to the right of the critical diameter. The claim follows from the additional observation that the curvature is negative for $D = D_{\mathrm{dry}}$, converges to 0 from above as $D \to \infty$, and (by Descartes) has a unique local extremum for $D > D_{\mathrm{dry}}$. ■

Finally, information about variations in the shape across the family of Köhler curves follows from the following lemma.

Lemma 2.6. *The slope of the graph of* $q(D; D_{\mathrm{dry}})$ *for a fixed value of* $q(D; D_{\mathrm{dry}})$ *is a decreasing function of* D_{dry} *to the left of* D_{crit} *and an increasing function of* D_{dry} *to the right of* D_{crit}.

Proof. The substitution $D = D(D_{\mathrm{dry}})$ into $q(D; D_{\mathrm{dry}})$ yields a constant function of D_{dry} provided that

$$(2.14) \qquad \frac{d}{dD_{\mathrm{dry}}} D(D_{\mathrm{dry}}) = -\frac{\partial_{D_{\mathrm{dry}}} q(D(D_{\mathrm{dry}}); D_{\mathrm{dry}})}{\partial_D q(D(D_{\mathrm{dry}}); D_{\mathrm{dry}})}.$$

Now consider the rate of change of $\partial_D q(D(D_{\mathrm{dry}}); D_{\mathrm{dry}})$ with respect to D_{dry}, obtained by the use of the chain rule and substitution of (2.14), and suppose that $\kappa < 1.4$. Using Descartes's

rule, we conclude that the sign of this quantity is opposite that of the slope of $q\left(D; D_{\mathrm{dry}}\right)$ evaluated at $D = D\left(D_{\mathrm{dry}}\right)$, and the claim follows. ∎

Corollary 2.7. The magnitude of the slope of $q\left(D; D_{\mathrm{dry}}\right)$ for a fixed value of $q\left(D; D_{\mathrm{dry}}\right)$ is a decreasing function of D_{dry} for all $D > D_{\mathrm{dry}}$ away from D_{crit}.

Corollary 2.8. Suppose that $D_{1,\mathrm{dry}} < D_{2,\mathrm{dry}}$, and consider $D_1 < D_{1,\mathrm{crit}}$ and $D_2 > D_{2,\mathrm{crit}}$, such that

$$(2.15) \qquad q\left(D_1; D_{1,\mathrm{dry}}\right) = q\left(D_2; D_{2,\mathrm{dry}}\right).$$

It follows that

$$(2.16) \qquad r\left(D_1\right) \partial_D q\left(D_1; D_{1,\mathrm{dry}}\right) > -r\left(D_2\right) \partial_D q\left(D_2; D_{2,\mathrm{dry}}\right).$$

2.2.2. Equilibria and bifurcations. Our interest lies ultimately in parameterizations of the fraction of droplet-forming particles, given physical processes of condensation and absorption, starting with the deposition of dry aerosol particles within the adiabatic control volume. It follows from (2.8) and (2.13) that, all other things being equal, $\dot{D}$ increases with dry diameter. Particles must thus remain ordered in size for all time according to their initial dry diameters. We refer to the set of points *compatible with the initial dry diameters* as the subset of state space where the ordering of the wet diameters agrees with the ordering of the dry diameters. In this section, however, we consider more broadly the dynamics of growth based at initial conditions compatible with the conservation of available humidity, but not necessarily with $D(D_{\mathrm{dry}}, 0) = D_{\mathrm{dry}}$. Where possible, we comment on the transient behavior expected in this special case.

For fixed S, it is clear from (2.8) that equilibrium is obtained for $D = D_{\mathrm{eq}}$, where the *equilibrium diameter D_{eq}* must satisfy

$$(2.17) \qquad S = q\left(D_{\mathrm{eq}}; D_{\mathrm{dry}}\right).$$

Since $\partial_D q\left(D; D_{\mathrm{dry}}\right)$ is positive for $D < D_{\mathrm{crit}}$ and negative for $D > D_{\mathrm{crit}}$, the equilibrium diameters $D_{\mathrm{eq}} < D_{\mathrm{crit}}$ are asymptotically stable, whereas those with $D_{\mathrm{eq}} > D_{\mathrm{crit}}$ are unstable. For $D_{\mathrm{eq}} = D_{\mathrm{crit}}$, we obtain a saddle-node equilibrium. The direction of the flow in D (for different fixed values of S) is indicated in Figure 2. In particular, we see unbounded growth in D for D greater than the unstable equilibrium diameter when $1 < S \leq q\left(D_{\mathrm{crit}}; D_{\mathrm{dry}}\right)$ and for all D when $S > q\left(D_{\mathrm{crit}}; D_{\mathrm{dry}}\right)$. In contrast, for $0 < S \leq 1$, the unique equilibrium diameter is globally attracting.

In the general autonomous case under consideration, however, S is not constant, but varies according to the differential equation

$$(2.18) \qquad \dot{S} = -\frac{3\hat{\gamma}}{N_{\mathrm{p}}} \sum_{i=1}^{N_{\mathrm{P}}} D_i^2 \dot{D}_i$$

for some positive constant $\hat{\gamma}$ (scaled relative to γ in (2.4) by P_{dry}), modeling the condensation and evaporation of water vapor onto/from individual aerosol particles. The negative feedback on the rate of change of S associated with growth of the wet diameter of any of the aerosol
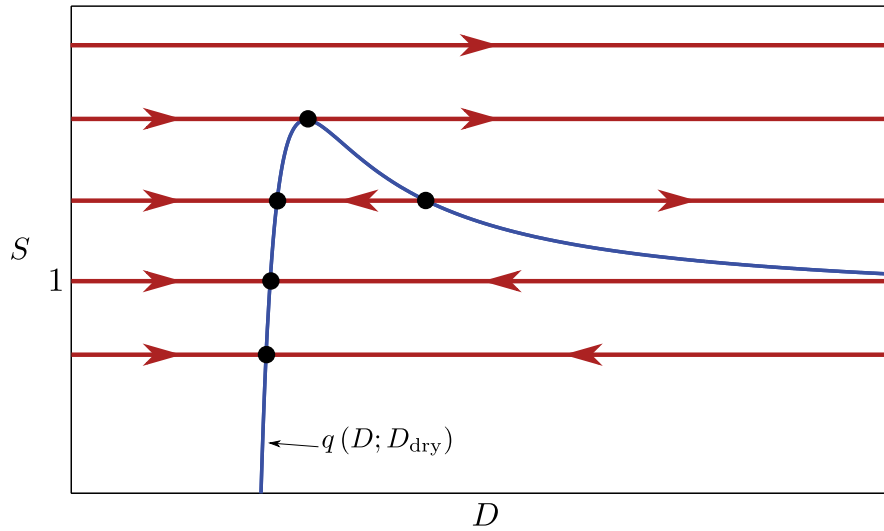
Figure 2. *For fixed values of S, the dynamics of individual particle diameters are described by the horizontal flow shown in the figure. For S below the critical saturation ratio, the transient dynamics approach equilibria located at intersections with the corresponding Köhler curve. For S above the critical saturation ratio, unbounded growth occurs. Equilibrium diameters below the supersaturation point are asymptotically stable, whereas those above the supersaturation point are unstable.*

particles makes unbounded growth impossible and thus sets the stage for a possible cessation or reversal of growth.

From (2.18), we obtain the *conservation law*

$$(2.19) \qquad S - S_{\mathrm{dry}} = -\frac{\hat{\gamma}}{N_{\mathrm{p}}} \sum_{i=1}^{N_{\mathrm{p}}} \left(D_i^3 - D_{i,\mathrm{dry}}^3 \right),$$

where S_{dry} again denotes the relative humidity when the dry aerosol particles are deposited in the control volume. It follows that the variations in wet diameter for N_{p} cloud-condensation nuclei are governed by the closed system of differential equations

$$(2.20) \qquad \dot{D}_i = r\left(D_i\right) \left(S_{\mathrm{dry}} - \frac{\hat{\gamma}}{N_{\mathrm{p}}} \sum_{j=1}^{N_{\mathrm{p}}} \left(D_j^3 - D_{j,\mathrm{dry}}^3 \right) - q\left(D_i; D_{i,\mathrm{dry}}\right) \right)$$

for $i = 1, \ldots, N_{\mathrm{p}}$.

Consider, at first, the case of $N_{\mathrm{p}} = 1$ and the single differential equation

$$(2.21) \qquad \dot{D} = r\left(D\right) \left(S_{\mathrm{dry}} - \hat{\gamma} \left(D^3 - D_{\mathrm{dry}}^3 \right) - q\left(D; D_{\mathrm{dry}}\right) \right),$$

where we have omitted the trivial subscript. Equilibrium is obtained for $D = D_{\mathrm{eq}}$, provided that

$$(2.22) \qquad S_{\mathrm{dry}} = \hat{\gamma} \left(D_{\mathrm{eq}}^3 - D_{\mathrm{dry}}^3 \right) + q\left(D_{\mathrm{eq}}; D_{\mathrm{dry}}\right).$$

Lemma 2.9. *For a given initial dry diameter D_{dry}, there exists a critical value $\hat{\gamma}^*$, such that all equilibria of the dynamical system in* (2.21) *are globally attractive provided that $\hat{\gamma} > \hat{\gamma}^*$ (see Figure 3). For $\hat{\gamma} < \hat{\gamma}^*$, there exist two critical values of S_{dry}, denoted by S_{dry}^* and S_{dry}^{**}, where $1 < S_{\mathrm{dry}}^* < S_{\mathrm{dry}}^{**}$, such that*

- *for $0 < S_{\mathrm{dry}} < S_{\mathrm{dry}}^*$, there exists a unique globally attractive equilibrium with $D_{\mathrm{eq}} < D_{\mathrm{crit}}$;*
- *for $S_{\mathrm{dry}}^{**} < S_{\mathrm{dry}}$, there exists a unique globally attractive equilibrium with $D_{\mathrm{eq}} > D_{\mathrm{crit}}$;*
- *for $S_{\mathrm{dry}}^* < S_{\mathrm{dry}} < S_{\mathrm{dry}}^{**}$, there exist two locally attractive equilibria with $D_{\mathrm{eq}} < D_{\mathrm{crit}}$ and $D_{\mathrm{eq}} > D_{\mathrm{crit}}$, respectively, separated by an unstable equilibrium with $D_{\mathrm{eq}} > D_{\mathrm{crit}}$.*

Proof. An equilibrium $D = D_{\mathrm{eq}}$ of the dynamical system in (2.21) is asymptotically stable when

$$(2.23) \qquad \hat{\gamma} > -\frac{\partial_D q\left(D_{\mathrm{eq}}; D_{\mathrm{dry}}\right)}{3D_{\mathrm{eq}}^2}$$

and unstable when the opposite inequality holds. The expression on the right-hand side is negative for $D_{\mathrm{eq}} < D_{\mathrm{crit}}$, is positive for $D_{\mathrm{eq}} > D_{\mathrm{crit}}$, and converges to 0 as $D_{\mathrm{eq}} \to \infty$. It follows that it must attain a local maximum for some $D_{\mathrm{eq}} > D_{\mathrm{dry}}$. As in the proof to Lemma 2.1, by Descartes's rule, the total number of local extrema for $D_{\mathrm{eq}} > D_{\mathrm{dry}}$ is bounded from above by the number of sign changes in the sequence

$$1,\ 48 + (4\kappa + 6)\tilde{\beta} - \kappa\tilde{\beta}^2,\ 168 + (4\kappa + 6)\tilde{\beta} - (\kappa + 6)\tilde{\beta}^2,$$
$$1008\kappa + (8\kappa^2 - 30\kappa - 108)\tilde{\beta} - (\kappa^2 + 36\kappa + 27)\tilde{\beta}^2,$$
$$1260\kappa + (2\kappa^2 - 60\kappa - 432)\tilde{\beta} - (30\kappa + 81)\tilde{\beta}^2,$$
$$168\kappa - (7\kappa + 126)\tilde{\beta} - (2\kappa + 18)\tilde{\beta}^2,$$
$$504\kappa - (14\kappa + 756)\tilde{\beta} - (2\kappa + 81)\tilde{\beta}^2,$$
$$72\kappa - (\kappa + 234)\tilde{\beta} - 18\tilde{\beta}^2,\ 2\kappa - 20\tilde{\beta} - \tilde{\beta}^2,\ -1$$

for $\tilde{\beta} > 0$. For $\kappa < 1.4$, this number equals 1, and the claim follows. ∎

The critical values S_{dry}^* and S_{dry}^{**} correspond to saddle-node bifurcations, where the branch of unstable equilibria meets each of the branches of stable equilibria. In particular, $S_{\mathrm{dry}}^* \to 1$ and $S_{\mathrm{dry}}^{**} \to q\left(D_{\mathrm{crit}}; D_{\mathrm{dry}}\right)$ as $\hat{\gamma} \to 0$.

Corollary 2.10. *The value $\hat{\gamma} = \hat{\gamma}^*$ corresponds to a cusp bifurcation, at which the two saddle-node bifurcations merge.*

In the one-particle case, the unbounded growth, obtained for sufficiently large values of S_{dry} when $\hat{\gamma} = 0$, is halted when $\hat{\gamma} > 0$ by the finiteness of the supply of water vapor. In the case of the initial condition $D(0) = D_{\mathrm{dry}}$, we find transient behavior to an equilibrium diameter corresponding to the leftmost point of intersection between the graph of $q(D, D_{\mathrm{dry}})$ and the graph of $S_{\mathrm{dry}} - \hat{\gamma}(D^3 - D_{\mathrm{dry}}^3)$. As seen in the left panel of Figure 3, for $\hat{\gamma} < \hat{\gamma}^*$, the transient dynamics converge to an equilibrium diameter below D_{crit} when $0 < S < S_{\mathrm{dry}}^{**}$ and to an equilibrium diameter above some lower bound greater than D_{crit} when $S > S_{\mathrm{dry}}^{**}$.
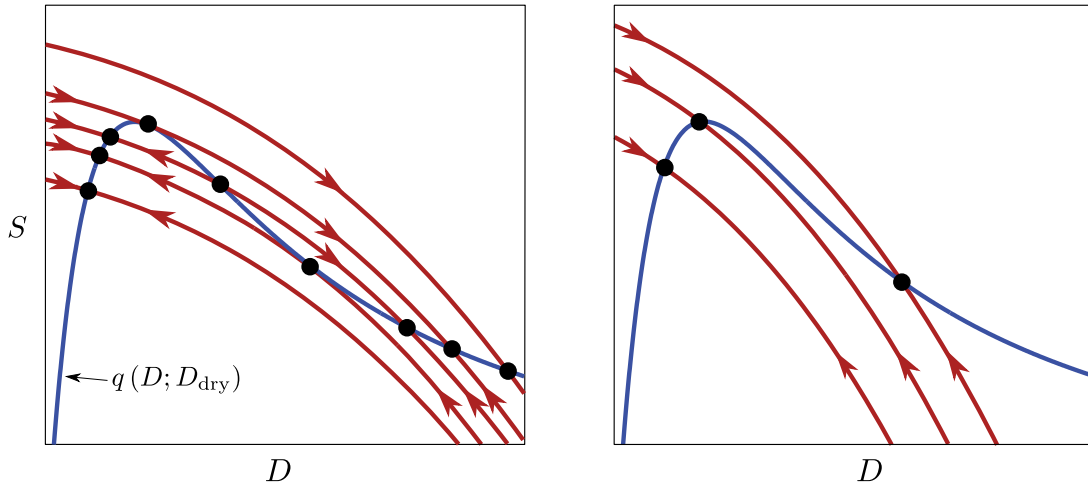
Figure 3. *State-space trajectories and the arrangement of equilibria, when $N_{\mathrm{p}} = 1$, for different values of S_{dry} in the case when $\hat{\gamma} < \hat{\gamma}^*$ (left panel) and $\hat{\gamma} > \hat{\gamma}^*$ (right panel), as described in Lemma 2.9.*

We consider next the case of $N_{\mathrm{p}} = 2$ and the two coupled differential equations

$$(2.24\mathrm{a}) \qquad \dot{D}_1 = r\left(D_1\right)\left(S_{\mathrm{dry}} - \frac{\hat{\gamma}}{2}\left(D_1^3 - D_{1,\mathrm{dry}}^3\right) - \frac{\hat{\gamma}}{2}\left(D_2^3 - D_{2,\mathrm{dry}}^3\right) - q\left(D_1; D_{1,\mathrm{dry}}\right)\right),$$

$$(2.24\mathrm{b}) \qquad \dot{D}_2 = r\left(D_2\right)\left(S_{\mathrm{dry}} - \frac{\hat{\gamma}}{2}\left(D_1^3 - D_{1,\mathrm{dry}}^3\right) - \frac{\hat{\gamma}}{2}\left(D_2^3 - D_{2,\mathrm{dry}}^3\right) - q\left(D_2; D_{2,\mathrm{dry}}\right)\right)$$

and assume without loss of generality that $D_{1,\mathrm{dry}} < D_{2,\mathrm{dry}}$. Equilibrium is obtained at $D_1 = D_{1,\mathrm{eq}}$ and $D_2 = D_{2,\mathrm{eq}}$ provided that $q\left(D_{1,\mathrm{eq}}; D_{1,\mathrm{dry}}\right) = q\left(D_{2,\mathrm{eq}}; D_{2,\mathrm{dry}}\right)$, in which case the corresponding value of S_{dry} may be obtained, for example, from

$$(2.25) \qquad S_{\mathrm{dry}} = \frac{\hat{\gamma}}{2}\left(D_{1,\mathrm{eq}}^3 - D_{1,\mathrm{dry}}^3\right) + \frac{\hat{\gamma}}{2}\left(D_{2,\mathrm{eq}}^3 - D_{2,\mathrm{dry}}^3\right) + q\left(D_{1,\mathrm{eq}}; D_{1,\mathrm{dry}}\right).$$

From (2.13) it follows that there exist two disjoint families of equilibria with $D_{1,\mathrm{eq}} < D_{1,\mathrm{crit}}$ and $D_{1,\mathrm{eq}} > D_{1,\mathrm{crit}}$, respectively, as shown in the two panels in Figure 4. From the earlier discussion about the ordering of particle sizes, we conclude that only the former of these two families is compatible with the initial dry diameters, independently of the value of S_{dry}.

While the discussion prior to (2.25) establishes necessary conditions for the existence of equilibria, sufficient conditions are given in the following lemma.

Lemma 2.11. *For given initial dry diameters $D_{1,\mathrm{dry}}$ and $D_{2,\mathrm{dry}}$, there exists a critical value $\hat{\gamma}^*$, such that all equilibria of the dynamical system in (2.24a)–(2.24b) that are compatible with the initial dry diameters are globally attractive provided that $\hat{\gamma} > \hat{\gamma}^*$. For $\hat{\gamma} < \hat{\gamma}^*$, there exist two critical values of S_{dry}, denoted by S_{dry}^* and S_{dry}^{**}, where $1 < S_{\mathrm{dry}}^* < S_{\mathrm{dry}}^{**}$, such that*

- *for $0 < S_{\mathrm{dry}} < S_{\mathrm{dry}}^*$, there exists a unique globally attractive equilibrium with $D_{2,\mathrm{eq}} < D_{2,\mathrm{crit}}$;*
- *for $S_{\mathrm{dry}}^{**} < S_{\mathrm{dry}}$, there exists a unique globally attractive equilibrium with $D_{2,\mathrm{eq}} > D_{2,\mathrm{crit}}$;*
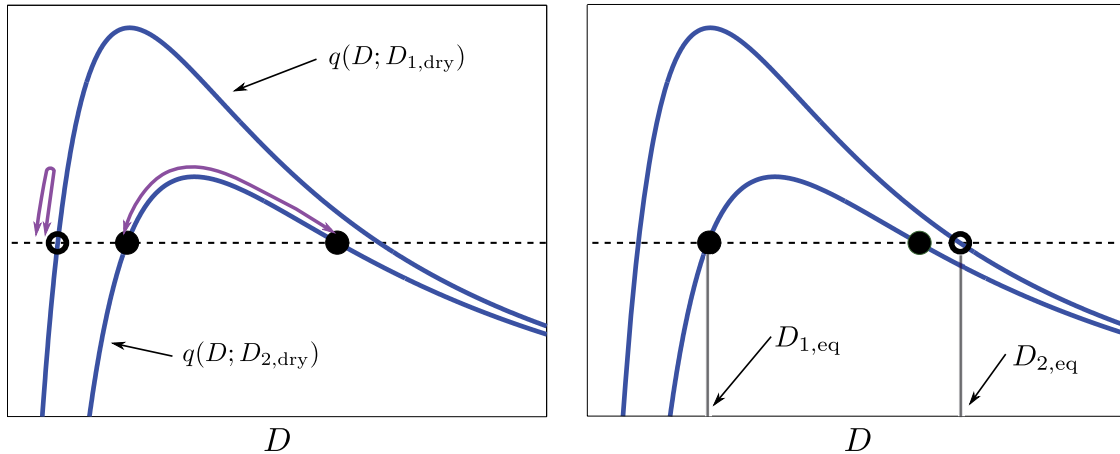
Figure 4. *Equilibrium configurations for the case when $N_p = 2$. Each equilibrium corresponds to a combination of wet diameters with identical vertical coordinates along the corresponding Köhler curves. There exist two disjoint families of equilibria with $D_{1,\text{eq}} < D_{1,\text{crit}}$ (left panel) and $D_{1,\text{eq}} > D_{1,\text{crit}}$ (right panel), respectively, of which only the first is compatible with the initial dry diameters. Note that the two possible equilibrium configurations in each of the two panels correspond to different values of S_{dry}, as may be obtained from (2.25). Purple curves indicate continuous transformation from one equilibrium to another.*

- *for $S_{\text{dry}}^* < S_{\text{dry}} < S_{\text{dry}}^{**}$, there exist two locally attractive equilibria with $D_{2,\text{eq}} < D_{2,\text{crit}}$ and $D_{2,\text{eq}} > D_{2,\text{crit}}$, respectively, separated by an unstable equilibrium with $D_{2,\text{eq}} > D_{2,\text{crit}}$.*

Proof. Let $q_i' := \partial_D q\,(D_{i,\text{eq}}; D_{1,\text{dry}})$ and $r_i := r\,(D_{i,\text{eq}})$. Using the result of Corollary 2.8 and the Hurwitz criterion for the negative stability of the Jacobian of the vector field corresponding to (2.24a)–(2.24b), local asymptotic stability of an equilibrium is obtained provided that the determinant

$$(2.26) \qquad r_1 r_2 \left(\frac{3}{2} D_{1,\text{eq}}^2 q_2' \hat{\gamma} + q_1' \left(q_2' + \frac{3}{2} D_{2,\text{eq}}^2 \hat{\gamma} \right) \right)$$

is positive, while the equilibrium is unstable when this quantity is negative. Equivalently, local asymptotic stability follows when

$$(2.27) \qquad \frac{\hat{\gamma} q_1'}{3 D_{1,\text{eq}}^2 \hat{\gamma} + 2 q_1'} > -\frac{q_2'}{3 D_{2,\text{eq}}^2},$$

which is always satisfied when (i) $D_{2,\text{eq}} < D_{2,\text{crit}}$, (ii) for sufficiently large $\hat{\gamma}$, independently of $D_{2,\text{eq}}$, and (iii) for sufficiently large $D_{2,\text{dry}} > D_{2,\text{crit}}$ for fixed $\hat{\gamma}$. For a given $D_{2,\text{eq}} > D_{2,\text{crit}}$, it is possible to select $\hat{\gamma}$, such that equality holds in (2.27), corresponding to a saddle-node bifurcation. For the same value of $\hat{\gamma}$, the inequality is satisfied in both of the limits $D_{2,\text{eq}} \to D_{2,\text{crit}}$ and $D_{2,\text{eq}} \to \infty$. It follows that a second saddle-node bifurcation must exist along the branch of equilibria for $D_{2,\text{eq}} > D_{2,\text{crit}}$. $\blacksquare$

By the conservation law in (2.19), it follows that the state-space dynamics may be viewed along an invariant two-dimensional manifold in the (D_1, D_2, S) space (cf. Figure 5) or (by projection) in the (D_1, D_2) plane (cf. Figure 6). In the former illustration, the D_1 and D_2
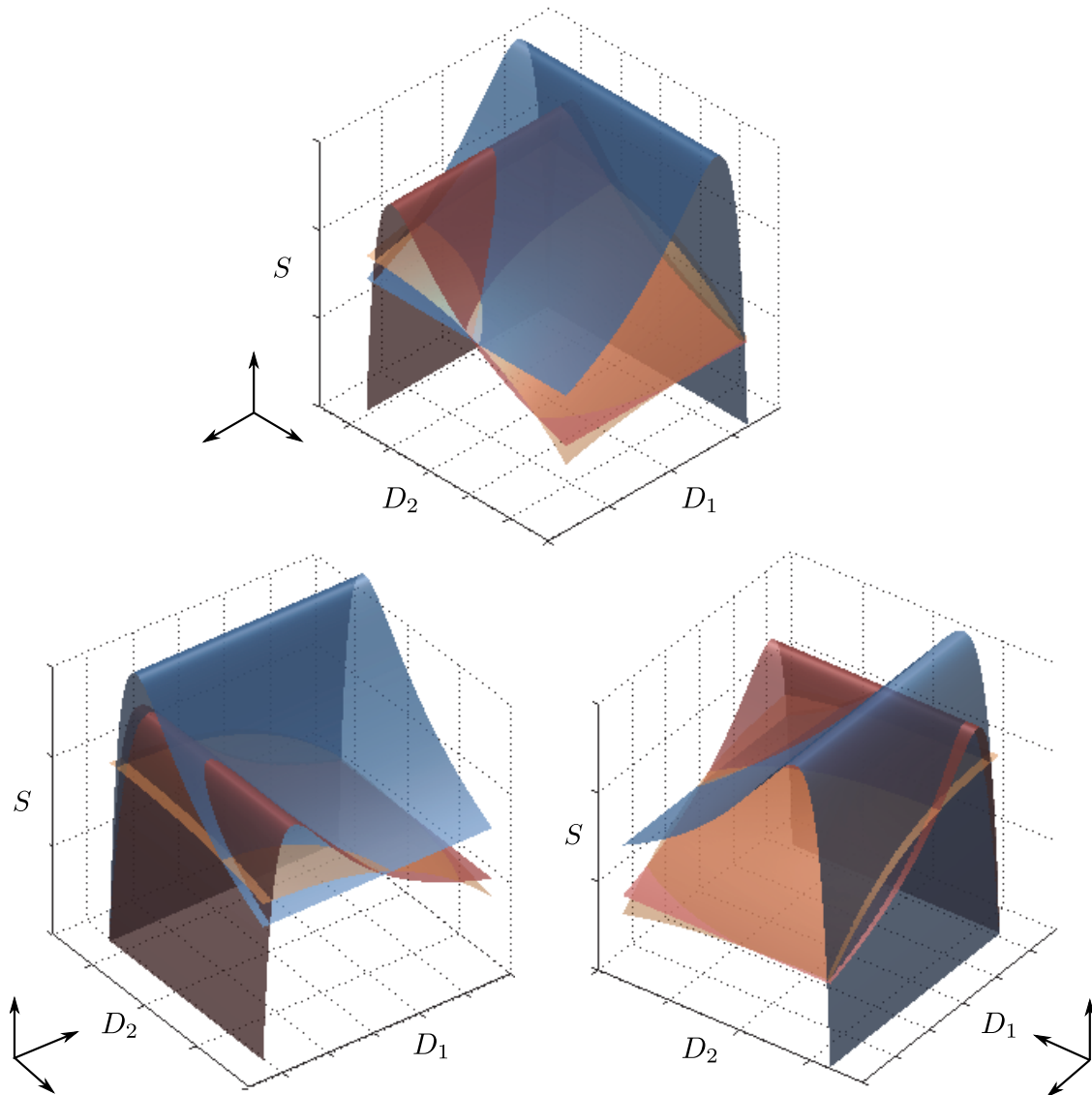
Figure 5. *When $N_\mathrm{p} = 2$, the system dynamics evolve on an invariant manifold (orange) in (D_1, D_2, S). Equilibria are located at the intersections of the invariant manifold with the nullsurfaces given by $S = q(D_1, D_{1,\mathrm{dry}})$ (red) and $S = q(D_2, D_{2,\mathrm{dry}})$ (blue).*

nullsurfaces (blue and red) are shown together with the invariant manifold (orange). Equilibria are found at the intersections between all three surfaces. In this case, the set of points compatible with the initial dry diameters corresponds to the subset $D_1 < D_2$. Transient dynamics based at the initial dry diameters converge to unique equilibria in this subset located at the "leftmost" intersection (in the value of D_2) of the invariant manifold with the two nullsurfaces.

In the general case of N_p particles, it is again true that $q\left(D_{i,\mathrm{eq}}; D_{i,\mathrm{dry}}\right)$ must be identical for
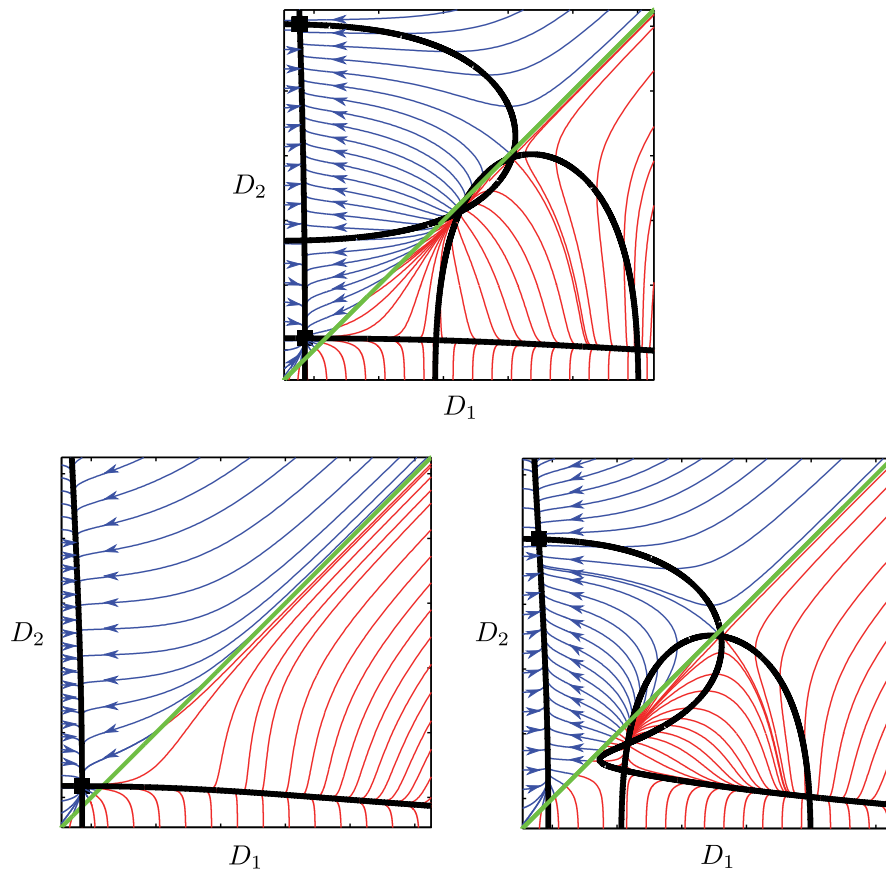
Figure 6. *Schematic of the projected state-space dynamics, when $N_{\mathrm{p}} = 2$, along the invariant manifold in the case that $\hat{\gamma} < \hat{\gamma}^*$ for $0 < S_{\mathrm{dry}} < S_{\mathrm{dry}}^*$ (lower left), $S_{\mathrm{dry}}^* < S_{\mathrm{dry}} < S_{\mathrm{dry}}^{**}$ (upper), and $S_{\mathrm{dry}} > S_{\mathrm{dry}}^{**}$ (lower right). Here, trajectory segments in the set of points compatible with the initial dry diameters (blue) are separated from segments that violate the condition that $D_1 < D_2$ (red) by the identity line (green). The intersections of the $\dot{D}_1 = 0$ and $\dot{D}_2 = 0$ nullsurfaces, respectively, with the invariant manifold are represented by the black curves. Equilibria occur at the intersections of these black curves.*

all $i = 1, \ldots, N_{\mathrm{p}}$ and that the corresponding value of S_{dry} may be obtained immediately after selection of $\hat{\gamma}$. Although there exist $2^{N_{\mathrm{p}}-1}$ families of equilibria, the only branch that is compatible with the initial dry diameters again corresponds to $D_{i,\mathrm{eq}} < D_{i,\mathrm{crit}}$ for $i = 1, \ldots, N_{\mathrm{p}}-1$, as illustrated in Figure 7 for the case with $N_{\mathrm{p}} = 3$. The corresponding determinant of the Jacobian of the vector field is found to equal

$$(2.28) \qquad \prod_{i=1}^{N_{\mathrm{p}}} r_i \prod_{j=1}^{N_{\mathrm{p}}} q_j' \left(1 + \frac{3\hat{\gamma}}{N_{\mathrm{p}}} \sum_{k=1}^{N_{\mathrm{p}}} \frac{D_{k,\mathrm{eq}}^2}{q_k'} \right).$$

An analysis similar to that in the proof of Lemma 2.11 may be used to establish the existence of two saddle-node bifurcations along the equilibrium branch for sufficiently small values of $\hat{\gamma}$.

The preceding analysis shows that regardless of the number of particles, a certain arrangement of particle sizes occurs in an equilibrium state that is a limit point of a trajectory
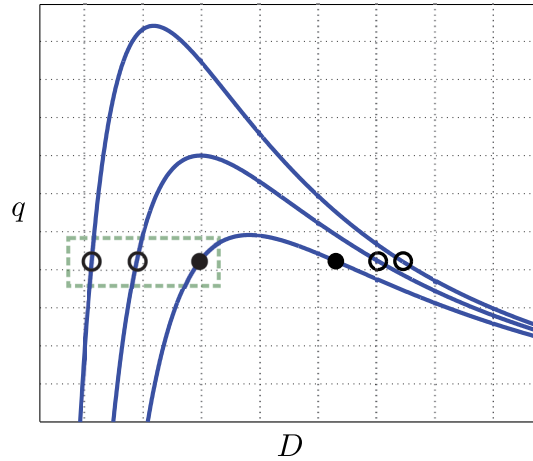
Figure 7. *Equilibrium configurations for the case when $N_{\mathrm{p}} = 3$. Each equilibrium corresponds to a combination of wet diameters with identical vertical coordinates along the corresponding Köhler curves. There exist four disjoint families of equilibria with different arrangements of the equilibrium diameters relative to the supersaturation points. Only the family with $D_{1,\mathrm{eq}} < D_{1,\mathrm{crit}}$ and $D_{2,\mathrm{eq}} < D_{2,\mathrm{crit}}$ is compatible with the initial dry diameters. An example equilibrium configuration is enclosed in the green box.*

based at the initial dry diameters. In particular, the largest particle, corresponding to the largest dry diameter, is the only one that may take a relativity large equilibrium diameter, while all other particles reach equilibrium at small diameters close to their corresponding dry diameters.

2.3. Nonautonomous dynamics. For the general study of the formation of droplets from cloud-condensation nuclei, it is necessary to account for temporal variations in temperature—for example, associated with vertical motion in the atmosphere [11]. In this case, the time-dependence $S(t)$ of the relative humidity is related to the distribution of wet diameters through the equation

$$(2.29) \qquad \frac{d}{dt}\left(P(T)S\right) = -\frac{3\gamma}{N_{\mathrm{p}}}\sum_{i=1}^{N_{\mathrm{p}}} D_i^2 \dot{D}_i$$

or its integral

$$(2.30) \qquad P(T)S - P_{\mathrm{dry}}S_{\mathrm{dry}} = -\frac{\gamma}{N_{\mathrm{p}}}\sum_{i=1}^{N_{\mathrm{p}}}\left(D_i^3 - D_{i,\mathrm{dry}}^3\right),$$

where the saturation vapor pressure $P(T)$ is a known, monotonically increasing function of temperature, and S_{dry} and P_{dry} again denote the relative humidity and saturation vapor pressure associated with the original emission of dry aerosol particles. For a given temperature variation, we obtain a closed system of N_{p} differential equations for the variations in the aerosol wet diameters by solving (2.30) for S and substituting into (2.8), where now α_0, α_1, and β are known functions of temperature. As in the case of the autonomous dynamics, unbounded particle growth is impossible, since the magnitude of the right-hand side of (2.30) cannot

exceed $P_{dry}S_{dry}$. Prior to this, S must fall below 1, ensuring reversal of growth for sufficiently large particle diameters.

2.3.1. Activated particles. As observed previously, particles must remain ordered in size for all time according to their initial dry diameters, independently of the time-dependence of the relative humidity S or the ambient temperature T. Any characterization of the particle population in terms of bounds on the wet diameters at a certain time, or on the nature of their time histories, is therefore equivalent to an ordered partition of the initial size distribution. As an example, we may loosely speak of a cloud-condensation nucleus as *activated* if it exhibits run-away growth toward the formation of a cloud droplet. It follows that, at any moment in time, all the particles smaller than a nonactivated particle are nonactivated, and all the particles larger than an activated particle are also activated.

The transient growth of the aerosol particles may now be obtained by explicit substitution of a time profile for the temperature. While for slow enough variations in T, one expects the dynamics to be guided by those found for the system described by (2.20), this is no longer true in the event of a rapidly rising aerosol layer. As an example, a steady updraft motion of the aerosol layer corresponds, to first approximation, to a linear decrease of the temperature in time. This results in a decreasing saturation vapor pressure and, all other factors being equal, an increase in the relative humidity. For as long as the relative humidity exceeds the value of $q(D, T; D_{dry})$ of a particle of a given dry diameter D_{dry}, the corresponding aerosol diameter D grows at a nonzero rate until such a time that competition for the available water vapor results in a decrease of the relative humidity below the corresponding (time-dependent) Köhler curve.

2.3.2. A heuristic parameterization. We consider again an aerosol size distribution given by a density function f and the corresponding cumulative distribution F. We seek to arrive at a relationship between the fraction of activated particles $p := 1 - F(D_{dry}^*)$, expressed in terms of some critical dry diameter D_{dry}^*, and statistical properties of f.

Inspired by Pinsky et al. [34, 35], suppose that the distribution of wet particle diameters relaxes rapidly (independently of f and without concomitant changes to the relative humidity, such that $S(0) \lesssim S_{dry} = 1$) to one consisting of (i) a monodisperse aerosol size distribution with pN_p activated particles of identical size D significantly larger than the corresponding dry diameters, and (ii) a distribution of $(1-p)N_p$ particles whose diameters have equilibrated at values approximately equal to the corresponding dry diameters. In this case, we may expand (2.29) to obtain

$$(2.31) \qquad \dot{S} = \frac{1}{P(T)}\left(-3p\gamma D^2 \dot{D} - \partial_T P(T)\dot{T}S\right).$$

For $D \gg D_{dry}$, we may approximate $q(D, T; D_{dry})$ in (2.8) by 1,

$$(2.32) \qquad \dot{D} = \frac{\alpha_0(T)}{D}(S-1),$$

where we also neglect the correction associated with α_1. Furthermore, (2.30) yields

$$(2.33) \qquad D = \left(\frac{P_{dry} - P(T)S}{p\gamma}\right)^{\frac{1}{3}}.$$

Substitution into (2.31) then results in the scalar, nonautonomous differential equation

$$(2.34) \qquad \dot{\chi} = -\frac{1}{P(T)} \left(3p^{\frac{2}{3}} \gamma^{\frac{2}{3}} \alpha_0(T) H^{\frac{1}{3}} \chi - \partial_T P(T) \dot{T} (1 - \chi) \right),$$

where $\chi := 1 - S$,

$$(2.35) \qquad H = P_{\text{dry}} - P(T) + P(T)\chi,$$

and $T = T_{\text{dry}} - \zeta t$ for constant ζ. In the limit that $S(0) \uparrow 1$, it follows that $\dot{S}(0) > 0$. In this case, we define $\hat{S}$ as the value of S at the first moment that $\dot{S} = \dot{\chi} = 0$, and we let $\hat{T}$ denote the temperature when this condition is reached.

We make plausible the existence of such a maximum in the limit as $S(0) \uparrow 1$ (and, consequently, as $H(0) \downarrow 0$) by replacing $\alpha_0(T)$ with a positive constant α_0 (see also Appendix B for a related discussion of the analysis in Pinsky et al. [34, 35]). In this case, suppose that $\dot{\chi}$ is negative and bounded away from 0 for all time, such that $-\chi(t) > kt$ for some $k > 0$. Then, since

$$(2.36) \qquad \frac{dH}{dt} = -3p^{\frac{2}{3}} \gamma^{\frac{2}{3}} \alpha_0 H^{\frac{1}{3}} \chi,$$

it follows that

$$(2.37) \qquad H(t)^{1/3} \sim \sqrt{\left(\int_0^t -2\chi(\tau) \, d\tau \right)}.$$

By the assumptions on χ, the right-hand side is bounded from below by $\sqrt{k}t$. It follows that the first term in (2.34) must eventually exceed, in magnitude, the value of the second term in this equation, in contradiction with the assumptions on χ, and the claim follows.

We finally arrive at a closed, nonlinear boundary-value problem for the time history $S(t)$ and the unknown fraction p of activated particles by imposing a condition on D_{dry}^* that captures the nature of the initial inflationary relaxation phase. Activation of an aerosol particle of a given dry diameter, as defined by an apparent inflationary phase of growth of the wet aerosol diameter, requires that the relative humidity exceed the critical saturation ratio at the instant that the wet diameter coincides with the corresponding supersaturation point. If we approximate $q(D, T; D_{\text{dry}})$ by its restriction to $T = \hat{T}$, then a necessary, but not sufficient, condition for this to hold is that the maximum relative humidity $\hat{S}$ exceed the critical saturation ratio $q(D_{\text{crit}}, \hat{T}; D_{\text{dry}})$. We rely on this condition in a first approximation of the fraction of activated particles for given values of γ and the rate of decrease of the ambient temperature. Specifically, we assume that D_{dry}^* is implicitly defined by the pair of scalar equations

$$(2.38) \qquad q\big(D_{\text{crit}}, \hat{T}; D_{\text{dry}}^*\big) = \hat{S},$$

$$(2.39) \qquad \partial_D q\big(D_{\text{crit}}, \hat{T}; D_{\text{dry}}^*\big) = 0.$$

A fully parameterized model of the aerosol dynamics is obtained by the following explicit expressions for the saturation vapor pressure:

$$(2.40) \qquad P(T) := 611.2 \exp \left(7.45 \ln(10) \frac{T - 273.15}{T - 38} \right),$$

and the model coefficients

$$(2.41) \qquad \alpha_0(T) := \frac{4M_w D_v}{\rho_w RT} P(T),$$

$$(2.42) \qquad \alpha_1(T) := 2D_v \sqrt{\frac{2\pi M_w}{RT}},$$

$$(2.43) \qquad \beta(T) := \frac{4M_w \sigma_w}{\rho_w RT},$$

where σ_w is the water surface tension and

$$(2.44) \qquad D_v := 0.211 \cdot 10^{-4} \left(\frac{T}{273}\right)^{1.94}$$

is the diffusivity coefficient (in units of m^2/s). For this parameterization, the rate of change of $q(D, T; D_{\mathrm{dry}})$ with respect to T is everywhere negative. It follows that variations in T parameterize a foliation of Köhler curves. In particular, the critical supersaturation ratio is a decreasing function of temperature.

It follows from (2.34) that

$$(2.45) \qquad \hat{\chi}' = \frac{1}{P}\left(3\frac{p^{\frac{2}{3}}}{\zeta}\gamma^{\frac{2}{3}}\alpha_0 H^{\frac{1}{3}}\hat{\chi} - \partial_T P \left(1 - \hat{\chi}\right)\right),$$

where $\hat{\chi}\left(T_{\mathrm{dry}} - \zeta t\right) := \chi(t)$. We observe that the dynamics of $\hat{\chi}$ are parameterized by the ratio $p^{2/3}/\zeta$ governing the balance between depletion of the ambient humidity due to the growth of aerosol particles and the increase in the humidity due to a decreasing saturation vapor pressure, but not by either p or ζ separately. Each value of this ratio thus corresponds to a unique pair of values of $\hat{S}$ and $\hat{T}$, as illustrated in Figure 8. The two curves included in this figure correspond to projections of the one-dimensional solution manifold to the discretized boundary-value problem given by a collocation approximation of (2.45) with $\hat{\chi}(T_{\mathrm{dry}}) = \hat{\chi}'(\hat{T}) = 0$ in terms of an unknown piecewise-polynomial approximant of $\hat{\chi}$ on a fixed mesh with 15 equal-sized intervals and polynomial degree 5, and for unknown $\hat{T}$. The results show dramatic variations in the values of $\hat{S}$ and $\hat{T}$ for very small values of the ratio $p^{2/3}/\zeta$, corresponding to the sought-after maximum of S being reached only after a significant change in temperature. In the extreme case, for which $\hat{S}$ and/or $\hat{T}$ lie outside of physically meaningful ranges, the validity of the model formulation is naturally put in question. Consequently, with Figure 8 in mind, we restrict our attention below to values of the ratio $p^{2/3}/\zeta > 1$.

With $f = f_{\mathrm{l.n.}}$, $E_{\mathrm{l.n.}} = 7 \times 10^{-8}$, and $V_{\mathrm{l.n.}} = 1 \times 10^{-14}$, there exists a locally unique value of p that satisfies the nonlinear boundary-value problem defined above near the initial solution guess represented by the open circles in Figure 8. We obtain a one-parameter family of solutions for fixed fractions p by allowing simultaneous variations in $E_{\mathrm{l.n.}}$ and $V_{\mathrm{l.n.}}$, as illustrated by the result of numerical continuation in Figure 9.

3. A computational framework. The simplifying assumptions made in the heuristic derivation above tend to overestimate the number of activated particles, as they fail to account for the possibility that a particle, whose critical supersaturation ratio is less than the maximum
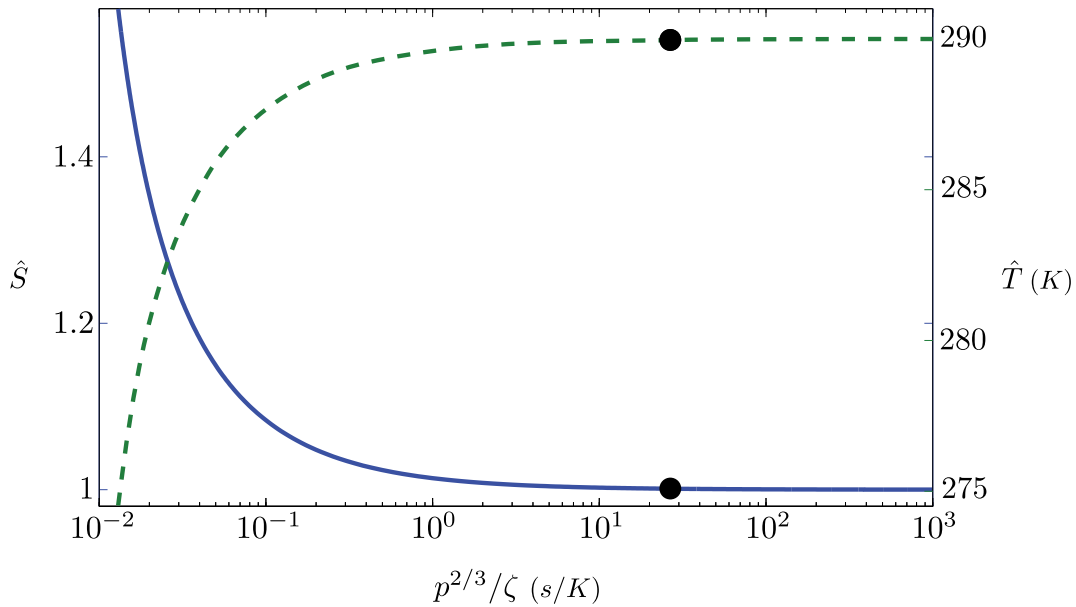
Figure 8. *The terminal values of relative humidity and temperature at the moment that the relative humidity reaches a local maximum parameterized by the ratio $p^{2/3}/\zeta$. Both $\hat{S}$ and $\hat{T}$ deviate dramatically from their physically meaningful ranges as $p^{2/3}/\zeta \to 0$. Here, the circle denotes the initial solution guess to the boundary-value problem obtained by imposing the additional conditions* (2.38)–(2.39) *with $\zeta = 0.01$, $E_{\mathrm{l.n.}} = 7 \times 10^{-8}$, $V_{\mathrm{l.n.}} = 1 \times 10^{-14}$, and $p = 1 - F_{\mathrm{l.n.}}(D^*_{\mathrm{dry}})$.*
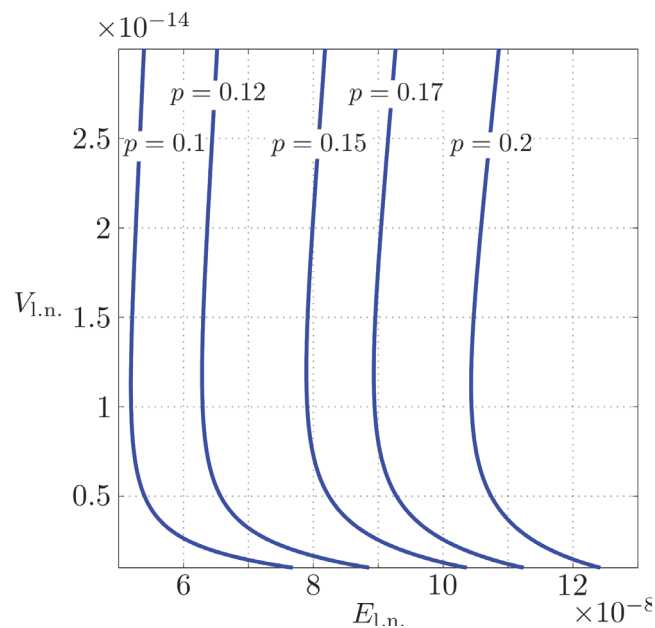
Figure 9. *Curves of constant fraction of activated particles, parameterized by pairs of values of the expectation $E_{\mathrm{l.n.}}$ and variance $V_{\mathrm{l.n.}}$, obtained using numerical continuation applied to a collocation discretization of the nonlinear boundary-value problem.*

relative humidity, nevertheless reaches a maximum diameter without undergoing an inflationary growth. This phenomenon is termed *kinetic limitation* [31], and particles affected by this phenomenon are said to be *kinetically limited*. As the error associated with this effect may be significant, it is important to evaluate its influence on predictions of the fraction of activated particles.

There are at least two relevant mechanisms that fall under the umbrella of kinetic limitation, for which we use the terminology in [31]. In the *evaporation mechanism*, the relative humidity drops below the critical saturation ratio of a given particle before the critical diameter D_{crit} is reached (see the left panel of Figure 10), resulting in the immediate *deactivation* of the particle. In the *deactivation mechanism*, shown in the right panel of Figure 10, the relative humidity exceeds the critical saturation ratio when the particle diameter reaches its critical value but falls below the corresponding Köhler curve shortly thereafter, after which evaporation again results in a shrinking diameter. A third mechanism [31], referred to as the *inertial mechanism*, describes particles of very large dry diameter and correspondingly very low critical supersaturation and large critical diameter. In this case, even though the critical diameter may not be reached, growth may continue for such a long time that, for practical purposes, the particles may be considered activated. The latter mechanism is outside the scope of our study and will not be considered here (but see [6, 22, 30] for work seeking to account for this effect).
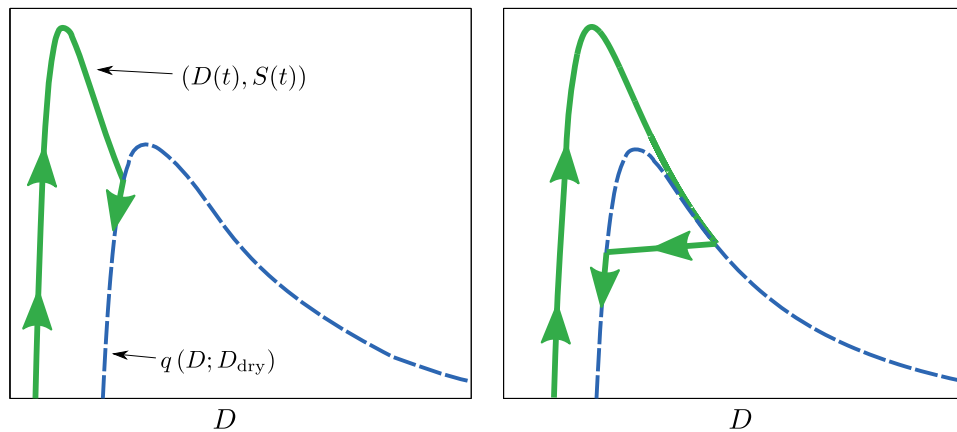
Figure 10. *Particles that experience a reversal of growth, even in the case that the maximum relative humidity along the projected trajectory (green) exceeds the critical saturation ratio along the corresponding D-nullcline (blue), are said to be kinetically limited. Here, reversal may occur before (left) or after (right) the corresponding supersaturation point.*

In lieu of the heuristic analysis in the previous section, we seek a systematic computational framework for the study of the dependence of the fraction of particles affected by kinetic limitation on the statistical properties of the initial distribution of dry diameters.

3.1. Forward simulation. As an example, we numerically analyze the dynamics of a collection of N_{p} particles with dry diameters defined by (2.7) for the case of the log-normal cumulative distribution in (2.2). In the numerical results reported throughout the remainder of the paper, $S_{\mathrm{dry}} = 0.98$, $T_{\mathrm{dry}} = 290$ K, and $\xi = 1/3000$.

Consider, specifically, a transient numerical simulation with $E_{\text{l.n.}} = 7 \times 10^{-8}$, $V_{\text{l.n.}} = 1 \times 10^{-14}$, $\zeta = 0.01$, and $N_{\text{p}} = 500$ integrated over 100 units of time. Let the initial conditions $S(0)$ and $D_i(0)$ be given by the relative humidity S_{eq} and distribution of diameters $D_{i,\text{eq}}$ corresponding to the asymptotically stable equilibrium below the critical supersaturation point obtained for constant temperature $T = T_{\text{dry}}$, the given distribution of dry diameters, and the corresponding relative humidity S_{dry}. It follows that

$$(3.1) \qquad S_{\text{eq}} - S_{\text{dry}} + \frac{\gamma}{P_{\text{dry}} N_{\text{p}}} \sum_{i=1}^{N_{\text{p}}} \left(D_{i,\text{eq}}^3 - D_{i,\text{dry}}^3 \right) = 0$$

and

$$(3.2) \qquad S_{\text{eq}} - q \left(D_{i,\text{eq}}, T_{\text{dry}}; D_{i,\text{dry}} \right) = 0$$

for $i = 1, \ldots, N_{\text{p}}$.

As seen from the resultant time histories in Figure 11, a subset of the particles, namely, those of sufficiently large dry diameter, exhibits an inflationary growth phase (around $t = 37$), after which the corresponding diameters continue to grow throughout the extent of the simulation. Particles with intermediate-size dry diameters are kinetically limited and fail to become activated, in spite of a brief inflationary phase. Finally, particles of sufficiently small dry diameters fail to enter an inflationary growth as the relative humidity never exceeds the corresponding critical saturation ratio. In the simulation, the 419th particle is the particle of largest dry diameter, for which the relative humidity does not exceed the corresponding critical saturation ratio. Similarly, the 430th particle is the particle of smallest dry diameter whose corresponding wet diameter continues to grow throughout the simulation. By the dynamically consistent ordering of diameters, it follows that particles 420 through 429 are all kinetically limited.

The time history $S(t)$ for the relative humidity shown in Figure 11 captures the collective influence on the availability of water vapor from the variations in the distribution of wet diameters approximated by the discretized particle model. We can use $S(t)$ (and the associated variations in temperature T) as an exogenous signal to drive the time history $D_0(t)$ of a test particle with dry diameter $D_{0,\text{dry}}$ according to (2.8). Note that $D_{0,\text{dry}}$ can take any value and is not ordered with respect to the values $D_{i,\text{dry}}$. A result of such an analysis is shown in Figure 12(upper panel). Here, the vertical axes represent the wet diameter $D_{0,\text{max}}$ and the elapsed time $t_{0,\text{max}}$ at an instant of vanishing right-hand side in (2.8), corresponding to a turning point in the growth of the corresponding wet diameter. These values coincide with the corresponding critical values $D_{i,\text{max}}$ and elapsed times $t_{i,\text{max}}$ in the discretized particle model, provided that $D_{0,\text{dry}} = D_{i,\text{dry}}$. As is evident in the figure, $D_{0,\text{max}}$ and $t_{0,\text{max}}$ depend sensitively on changes to the dry diameter $D_{0,\text{dry}}$ close to the transition to particles with inflationary growth (which fail to reach such an instant during the 100 units of integration time).

An alternative representation of the data in Figure 12(upper panel) is given in Figure 12(lower panel), where we observe a similar sensitivity in graphing the ratio $t_{0,\text{max}}/t_{429,\text{max}}$ versus the ratio $\hat{D}_0/\hat{D}_{429}$ of wet diameters at the instant that $\dot{S} = 0$. We generalize this observation to an arbitrary discretization of the initial distribution of dry diameters (and the corresponding time histories) by letting λ denote the slope at $(1, 1)$ of the graph of $t_{0,\text{max}}/t_{\text{last,max}}$
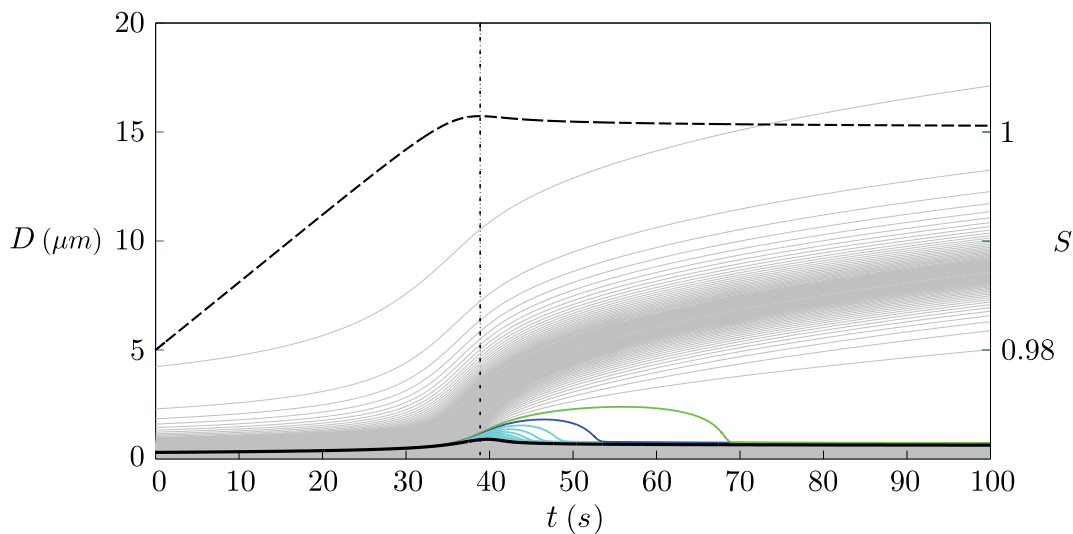
Figure 11. *Time histories for the wet diameters of 500 aerosol particles along with the corresponding relative humidity (dashed curve). Here, the vertical dotted line indicates the instant at which the relative humidity reaches its maximum value. Particles may be distinguished by their growth pattern; activated particles undergo a sudden increase in their wet diameters around the time of the peak in relative humidity and continue persistent growth past this time. Colored curves indicate kinetically limited particles that also experience initial rapid growth but reach a maximum diameter and then revert back close to their initial dry diameter. The thick black curve represents the particle with the largest dry diameter that is neither kinetically limited nor activated.*

versus $\hat{D}_0/\hat{D}_{\text{last}}$. Here, the subscript $_{\text{last}}$ represents the index of the largest particle to reach a maximum during the simulation. In particular, we argue that the discretized model resolves the transition between kinetically limited particles and fully activated particles with satisfactory detail provided that $\lambda \gg 1$. Notably, in the case of the data in Figure 12(lower panel), $\lambda \approx 15$. As a comparison, a similar analysis with $N_{\text{p}} = 3000$ (with the 429th particle replaced by the 2559 particle) results in $\lambda \approx 55$.

We finally comment on the convergence of the predicted fraction of activated particles associated with a refined discretization of the aerosol size distribution function. Based on the numerical data in Figure 13, we performed a least-squares fit of the model $\varepsilon_{\text{p}} := p - p^* = CN_{\text{p}}^r$, which resulted in model parameter values of $C = -3.759$, $r = -1.045$, and the limit $p^* = 0.1477$. This limiting value of p^* corresponds to the fraction that would be predicted by analysis of the integro-differential equation in (2.5), and the first-order convergence rate ($r \approx 1$) is consistent with the cumulatively uniform particle distribution produced by (2.7).

3.2. A boundary-value problem. Inspired by the time histories found using direct numerical simulation, we seek a boundary-value formulation such that every point on the corresponding solution manifold corresponds to the time histories of particles with the same fraction of activated, but not kinetically limited, particles. We consider two alternative heuristic criteria that each characterize an activated particle and explore the predicted fraction of kinetically limited particles under variations in the statistical moments of the initial distribution of dry aerosol diameters. In particular, given the discretization of the initial distribution of dry diameters in (2.7), let p denote the fraction of activated particles exhibiting run-away growth
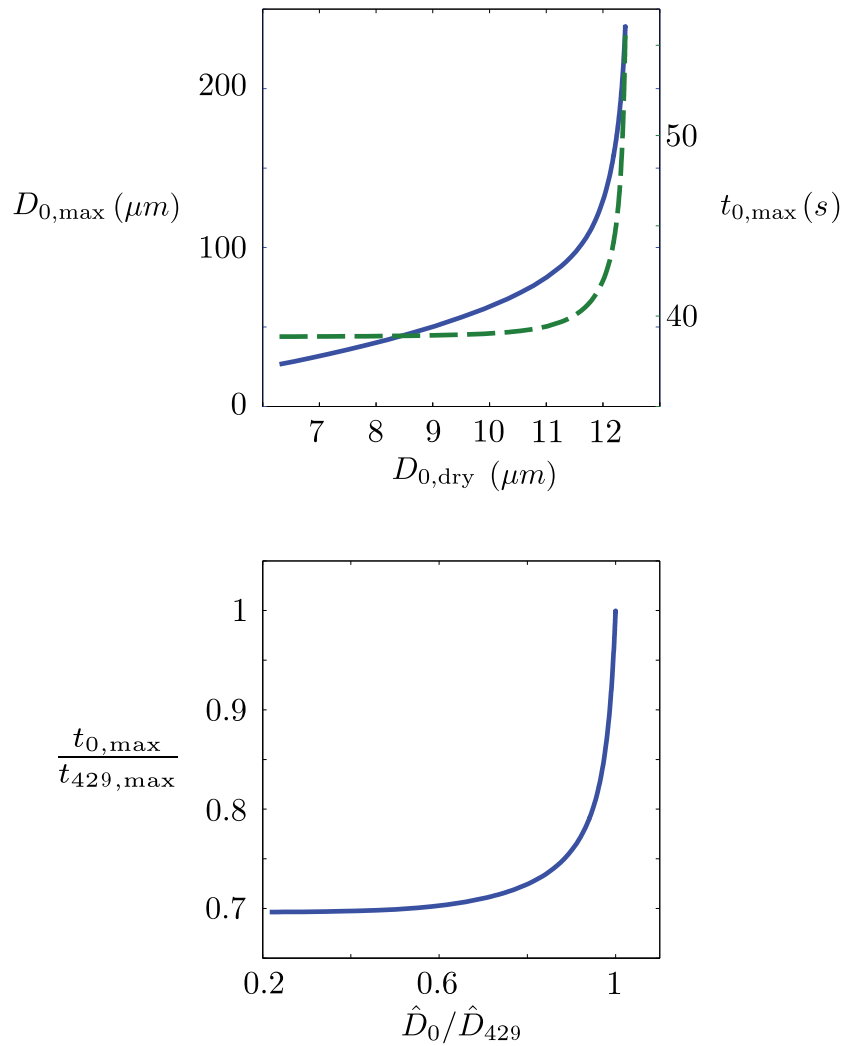
Figure 12. *(Upper) Variations in the maximum wet diameter (blue) and the corresponding time (green) parameterized by the corresponding dry diameter for a test particle whose dynamics is governed by the time history of the relative humidity in Figure 11. (Lower) The ratio of the elapsed time, at which the test particle reaches its maximum diameter, and the corresponding time for the largest kinetically limited particle versus the ratio of the corresponding wet diameters at the moment that the relative humidity reaches its maximum value. Note that the wet diameter of particles at their turning points undergoes a very steep change in a narrow region corresponding to dry diameters of particles that separate activated particles from others.*

throughout the duration of the relevant time histories. For an a priori value of p, it follows that the $_{\mathrm{last}}$ subscript represents a known particle index.

Now consider a three-stage segmentation of the continuous time histories of the relative humidity S, the wet aerosol diameters D_i, and the wet diameter D_0 of a test particle with $D_{0,\mathrm{dry}} = D_{\mathrm{last,dry}} - \delta$ for some $\delta > 0$. The first segment is characterized by initial conditions for S and D_i, for $i = 0, \ldots, N_{\mathrm{p}}$ coincident with the equilibrium values S_{eq} and $D_{i,\mathrm{eq}}$ (below the critical saturation point) obtained from (3.1) and (3.2), where the latter equation applies also
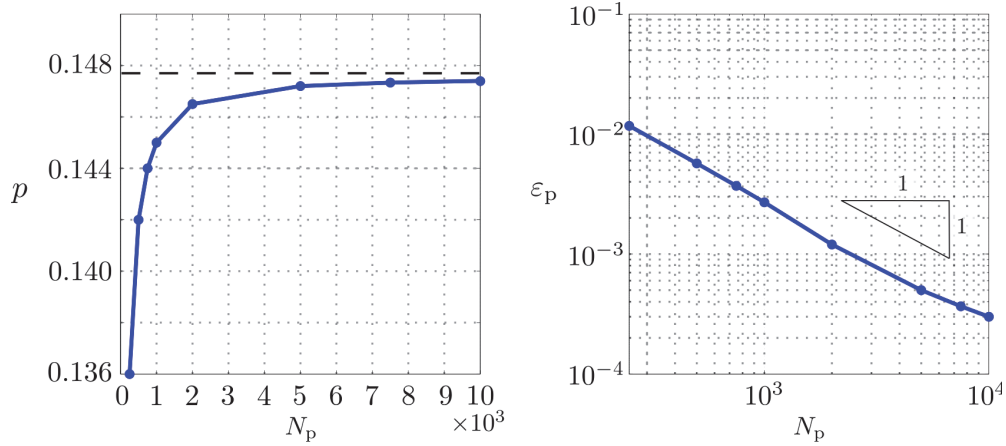
Figure 13. *The left panel shows the fraction of activated particles (p) as the number of particles (N_p) increases. The dashed line shows the numerically fitted converged value p^*. The right panel shows the number of particles versus the difference between the corresponding fraction of activated particles and the limiting value in a log-log plot.*

to $i = 0$. The first segment ends after an elapsed time $\hat{t}$ at a local maximum of $S(t)$. Similarly, the second and third segments are assumed to terminate after total elapsed times $t_{0,\mathrm{max}}$ and $t_{\mathrm{last,max}}$, at points where S equals $q\left(D_0, T; D_{0,\mathrm{dry}}\right)$ and $q\left(D_{\mathrm{last}}, T; D_{\mathrm{last,dry}}\right)$, respectively.

Let $\hat{S}$, $\hat{T}$, and $\hat{D}_i$ for $i = 0, \ldots, N_\mathrm{p}$ denote the relative humidity, ambient temperature, and particle diameters at $t = \hat{t}$. Then, a particle of dry radius $D_{i,\mathrm{dry}}$ is said to be activated *according to the first criterion* if $\hat{S}$ exceeds the critical saturation ratio $q(D_{\mathrm{crit}}, \hat{T}; D_{i,\mathrm{dry}})$. Alternatively (cf. [16]), a particle is said to be activated *according to the second criterion* if its diameter $\hat{D}_i$ exceeds the critical supersaturation point D_{crit} associated with the corresponding dry diameter $D_{i,\mathrm{dry}}$ and $T = \hat{T}$.

Finally, in order to ensure that the discretization resolves the transition between kinetically limited particles and fully activated particles with satisfactory detail, we impose the additional condition that the slope λ defined in the previous section, obtained here from a finite-difference approximation, equal some given large positive number λ^*. Collectively, the corresponding boundary conditions constitute algebraic constraints on the unknown time histories of the form

$$(3.3) \quad \begin{pmatrix} S(0) - S_{\mathrm{dry}} + \frac{\gamma}{P\left(T_{\mathrm{dry}}\right)N_\mathrm{p}} \sum_{i=1}^{N_\mathrm{p}} \left(D_i^3(0) - D_{i,\mathrm{dry}}^3\right) \\ S(0) - q\left(D_0(0), T_{\mathrm{dry}}; D_{0,\mathrm{dry}}\right) \\ \vdots \\ S(0) - q\left(D_{N_\mathrm{p}}(0), T_{\mathrm{dry}}; D_{N_\mathrm{p},\mathrm{dry}}\right) \\ \dot{S}\left(\hat{t}\right) \\ S\left(t_{0,\mathrm{max}}\right) - q\left(D_0\left(t_{0,\mathrm{max}}\right), T\left(t_{0,\mathrm{max}}\right); D_{0,\mathrm{dry}}\right) \\ S\left(t_{\mathrm{last,max}}\right) - q\left(D_{\mathrm{last}}\left(t_{\mathrm{last,max}}\right), T\left(t_{\mathrm{last,max}}\right); D_{\mathrm{last,dry}}\right) \\ \hat{D}_{\mathrm{last}}\left(t_{\mathrm{last,max}} - t_{0,\mathrm{max}}\right) - \lambda^* t_{\mathrm{last,max}}\left(\hat{D}_{\mathrm{last}} - \hat{D}_0\right) \end{pmatrix} = 0.$$

3.3. Discretization. In order that we obtain a one-parameter family of solutions to the boundary-value formulation in the previous section, we apply path-following techniques to a suitable discretization of the system of ordinary differential equations, using the MATLAB-based computational continuation core COCO. Specifically, we approximate each of the unknown time histories in terms of continuous, piecewise-polynomial functions, and we require that these satisfy the boundary conditions, as well as the governing differential equations at a collection of discrete collocation nodes (the so-called *collocation conditions*). Finally, we ensure that the number of unknown continuation variables exceeds the number of corresponding algebraic equations by one.

Given the natural segmentation of the boundary-value problem, we treat each of the segments separately and regain the original transient time histories by imposing continuity across the segment boundaries. On each segment, we shift and scale the time variable in order to obtain a system of differential equations on the interval $[0, 1]$, parameterized by the interval duration, per the following relationship:

$$(3.4) \qquad \frac{\mathrm{d}x(t)}{\mathrm{d}t} = f(x(t)), \quad t \in [t_b, t_e] \implies \frac{\mathrm{d}x(t(\tau))}{\mathrm{d}\tau} = (t_e - t_b)\, f(x(t(\tau))), \quad \tau \in [0, 1],$$

for $t(\tau) = t_b + \tau\,(t_e - t_b)$. On each segment, each scalar-valued, piecewise-polynomial approximant is naturally associated with a partition of the time domain in terms of a collection of *mesh nodes* and *mesh intervals*. We typically parameterize the approximant on each such interval in terms of a Lagrange interpolant through unknown values on a set of base points. The number of base points exceeds the polynomial degree by one.

An *asynchronous* mesh is characterized by more than one collection of mesh nodes across the set of approximants. When the union of all mesh nodes across the different approximants equals the mesh nodes for each of the approximants, we speak of a *synchronous* mesh. A synchronous mesh is said to be *uniform* if the mesh intervals are all equal in length and *nonuniform* otherwise. A mesh is *adaptive* if it is updated during continuation to ensure that an estimate of the discretization errors remains bounded below a critical threshold. Such updates may include changes to the location of individual nodes (r-type), as well as the number of mesh nodes or the size of the intervals (p-type and h-type, respectively).

The imposition of collocation conditions on the polynomial approximants requires the use of Lagrange interpolation in order to obtain algebraic conditions on the unknown base point values. In the case of a synchronous mesh, there exists a linear and variable-independent relationship between the values of the polynomial functions and their derivatives at the collocation nodes and base points, respectively. Mesh updates may be reduced to discrete changes to scaling constants in the collocation conditions, without any change to this linear relationship. In contrast, in an asynchronous mesh, each scalar-valued approximant is associated with a distinct such linear relationship. In this case, any updates to the individual meshes require recomputing the coefficients of the corresponding linear maps.

It is clear that the choice of mesh affects both the accuracy of the discretization as well as the computational cost associated with applying linear and nonlinear solvers to the discretized boundary-value problem. In the case of a sufficiently high-dimensional dynamical system, it is quite conceivable that the choice may affect the feasibility of the analysis, as the required intermediate storage exceeds available machine memory. Ultimately, the choice of mesh must

be guided by the observed nature of the relevant time histories. Large differences between the characteristic time scales for individual state variables at the same instant, between the characteristic time scales for a single state variable at different instants, or between the characteristic time scales for a single variable at the same instant but for different points on the solution manifold of the boundary-value problem suggest the use of asynchronous, nonuniform, and adaptive meshes, respectively.

For the analysis reported below of the aerosol boundary-value problem, we use an asynchronous, nonuniform, adaptive mesh in order to account for dissimilar growth rates and significant sensitivity in the behavior of kinetically limited particles to changes in the system parameters. The detailed implementation of the mesh selection and adaptation algorithm is discussed in Appendix A. Here, the state variables associated with the discretized distribution of particle diameters are further discretized in time according to three distinct meshes. For example, we could partition the variables such that the first of these describes particles whose diameters remain close to their initial diameters and exhibit relatively slow dynamics. Similarly, the second mesh could be designed to describe particles whose diameters exhibit more rapid variability, e.g., a sudden reduction in size following the termination of initial growth. The third mesh would then describe particles with relatively large dry diameters, which exhibit intermediate (and persistent) growth rates.

The algorithm introduced in Appendix A provides for an optimal partition of variables between the three meshes, provided that two variables with similar values in the accumulated estimated error have similar distributions of error along the relevant time histories. This condition is satisfied for all variables along the first segment, and for the activated and nonactivated particles along all segments. Along the second and third segments, however, we find that the kinetically limited particles violate this condition, as the corresponding phases of rapid variability occur with significant time separation for different particles. As these phases also translate significantly along the second and third segments during continuation, we choose to allocate all the kinetically limited particles to a single uniform mesh. The interval size is here chosen as the minimum interval size computed from the error equidistribution algorithm in Appendix A. For each adaptation step, the first kinetically limited particle is identified from the maximal value of the relative humidity and the corresponding critical saturation ratio. In all cases, we use a separate mesh for the piecewise-polynomial approximant of the relative humidity (noting that this is affected by all the different time scales present in the dynamics of the particle diameters).

3.4. Numerical results. We proceed to implement the asynchronous collocation scheme described in Appendix A with $m = 4$ and $TOL = 10^{-10}$. For each of the three cases reported below, an initial solution guess is obtained using forward simulation with MATLAB for $N_{\mathrm{p}} = 3000$, $V_{\mathrm{l.n.}} = 1 \times 10^{-14}$, and $E_{\mathrm{l.n.}} = 7 \times 10^{-8}$, 8×10^{-8}, 9×10^{-8}. The assignment of individual particle time histories to one of the three meshes and the number and location of the corresponding mesh nodes are updated adaptively every five continuation steps. In each case, a one-parameter family of solutions to the discretized boundary-value problem results by allowing two of the remaining model parameters to vary.

As an example, the left panel in Figure 14 shows the projection of the solution manifolds onto the $(E_{\mathrm{l.n.}}, V_{\mathrm{l.n.}})$ plane in the case that $\zeta = 0.01$ and for p equal to 0.147, 0.162, and 0.176,

respectively. Unexpectedly, these curves are straight lines going through the origin with slopes equal to 4.87×10^{-7}, 3.76×10^{-7}, and 3.14×10^{-7}, respectively. This suggests that if there exists a monotonically decreasing function that relates the fraction p of activated particles to the corresponding slope, then the value of p may be predicted directly from the expectation and variance of the original log-normal distribution. The right panel of Figure 14 shows the relative difference, ε_{k}, between the predicted fraction of activated particles using each of the heuristic criteria and $p = 0.147$ under variation in the expectation. As expected, in this case as well as the other two cases, both heuristic criteria overestimate the number of activated particles, with a larger fraction of particles activated according to the first criterion than those activated according to the second criterion. In the parameter ranges shown in Figure 14, the predicted values using the second criterion achieve a local maximum, while the prediction according to the first criterion increases monotonically with $E_{\mathrm{l.n.}}$.
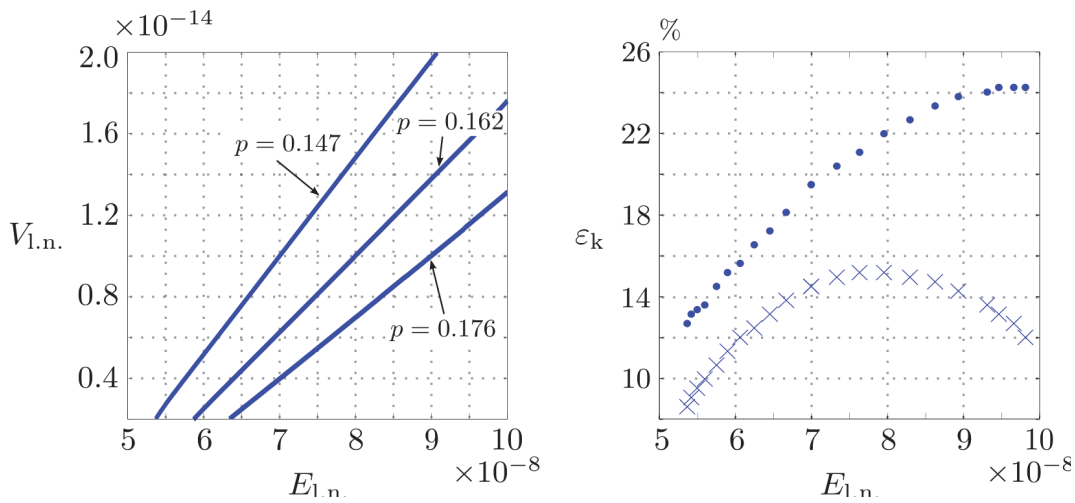
Figure 14. *The left panel shows families of pairs of expectation and variance for fixed p and ζ that satisfy the fully resolved formulation. The right panel shows the corresponding (normalized) difference between $p = 0.147$ and the predicted values obtained using the first (dots) and the second (crosses) heuristic criterion.*

For $p = 0.147$, the panels in Figure 15 show the relationships between the rate of temperature decay ζ and $E_{\mathrm{l.n.}}$ or $V_{\mathrm{l.n.}}$, respectively, along the corresponding solution manifold. As seen in panel (a), for fixed $V_{\mathrm{l.n.}}$, ζ increases with $E_{\mathrm{l.n.}}$ in order to maintain a fixed fraction of activated particles. In contrast, as seen in panel (b), for fixed $E_{\mathrm{l.n.}}$, ζ decreases with increasing values of $V_{\mathrm{l.n.}}$. The difference between the corresponding predictions of the fraction of activated particles according to each of the two heuristic criteria and the actual fraction are shown in panels (c) and (d). We note significant differences, associated with kinetically limited particles, between these predictions and the actual value of p. Indeed, the prediction error incurred by the first heuristic criterion grows with $E_{\mathrm{l.n.}}$ (and the associated reduction in the rate of temperature decay), whereas that incurred by the second heuristic criterion improves after an initial brief increase.

4. Concluding remarks. As argued in previous sections, the failure to account for the phenomenon of kinetic limitation may lead to overestimation of the fraction of activated particles
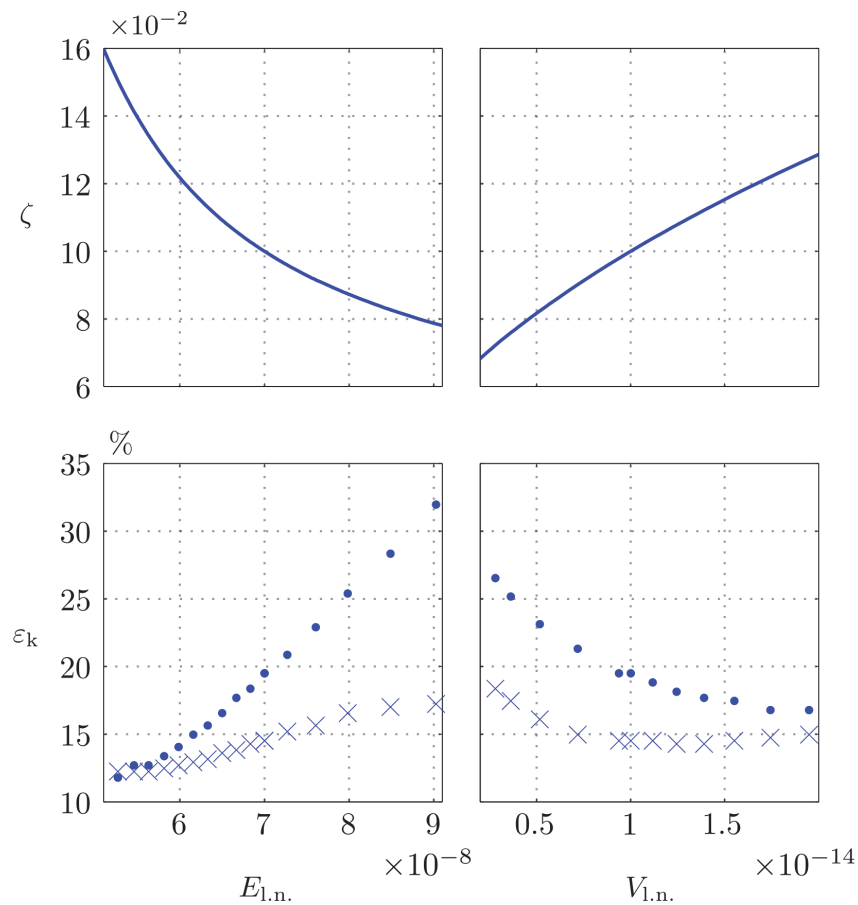
Figure 15. *The upper left panel shows families of pairs of expectation and the rate of temperature decay for fixed $p(= 0.147)$ and variance. The lower left panel shows the corresponding (normalized) difference between $p = 0.147$ and the predicted values of the fraction of activated particles obtained using the first (dots) and the second (crosses) criterion. The upper right and the lower right panels show the corresponding families for fixed $p(= 0.147)$ and $E_{\text{l.n.}}$.*

when using heuristic parameterization techniques. While the effect is broadly recognized, it is commonly neglected [16]. Forward simulation techniques avoid simplifying assumptions regarding the system dynamics or the application of heuristic threshold criteria but come at significant cost and provide no guidance for a systematic exploration of parameter dependence.

In contrast, the boundary-value formulation proposed in this work targets an inverse formalism in which a given fraction of activated particles is imposed upon the outcome of a transient time history. Root-finding techniques are then used to compute corresponding families of input parameters, e.g., pairs of expectations and variances for the initial distribution of dry diameters. This inverse framework affords a systematic study of combinations of model parameters that yield a predefined outcome. As seen in the previous section, the methodology yields insights regarding such combinations (notably the linear relationship between $E_{\text{l.n.}}$ and $V_{\text{l.n.}}$ for fixed values of p) that would not be readily available from a collection of forward

simulations.

Several remarks are in order regarding the choice of discretization of the boundary-value problem and the associated implementation of a nonlinear root-finding algorithm. First, we have chosen to rely on a Newton technique applied simultaneously to the entire vector of unknown base point values in the collocation paradigm, rather than a sequential, forward-shooting formalism, known for its sensitivity to local instability. As a consequence, the computational analysis is accompanied by significant memory demands and the possibility of exhausting available resources in the case of a high-dimensional system with a finely resolved temporal mesh.

Second, to accommodate constraints on computational resources, we have associated a separate temporal discretization to each group of state variables with characteristically similar time histories. Such an asynchronous discretization algorithm may lead to dramatic reductions in problem size, especially for slow-fast, large-scale dynamical systems. In the case at hand, it resulted in an order-of-magnitude reduction in the number of unknowns ($\sim 10^5$ compared to the synchronous mesh with $\sim 10^6$ unknowns and the case of a uniform, synchronous mesh with $\sim 10^7$ unknowns), allowing extensive numerical exploration and a finely resolved discretization of the distribution of dry particle diameters.

Finally, we have relied on an adaptive discretization scheme that accommodates changes in the properties of individual time histories during parameter continuation. In the absence of a rigorous error analysis, we used a mesh selection strategy that treats each mesh separately, without accounting for the influence of interpolation errors between meshes. A more sophisticated approach that would lend further credence to the numerical predictions should be based on theoretical estimates of error growth rates and the effect of coupling between meshes.

Appendix A. Asynchronous collocation. In this section, we develop the formulation for asynchronous discretization of a system of ordinary differential equations.

A.1. Discretization. Consider, in particular, the solution $y(t) \in \mathbb{R}^n$ on the interval $[0, T]$ to an ordinary differential equation of the form

$$(A.1) \qquad\qquad\qquad \dot{y} = f(y, p)$$

in terms of a vector field f and some choice of problem parameters $p \in \mathbb{R}^q$. Let $\{\{\kappa_{\alpha,j}\}_{j=1}^{N_\alpha}\}_{\alpha \in \mathcal{A}}$ denote a finite collection of sequences, such that

$$(A.2) \qquad\qquad\qquad \sum_{j=1}^{N_\alpha} \kappa_{\alpha,j} = 1 \quad \forall \alpha \in \mathcal{A}.$$

Each $\alpha \in \mathcal{A}$ corresponds to a partition

$$(A.3) \qquad \pi_\alpha: \quad 0 = t_{\alpha,0} < \cdots < t_{\alpha,j} = T \sum_{k=1}^{j} \kappa_{\alpha,k} < \cdots < t_{\alpha,N_\alpha} = T$$

of the interval $[0, T]$ in terms of the mesh nodes $t_{\alpha,j}$ for $j = 1, \ldots, N_\alpha$. For each i, we associate π_α, for some $\alpha \in \mathcal{A}$, to y_i by introducing a corresponding continuous approximant, defined

for $t \in [t_{\alpha,j}, t_{\alpha,j+1}]$ in terms of the independent variable

$$(A.4) \qquad \sigma := 2\frac{t - t_{\alpha,j}}{T\kappa_{\alpha,j+1}} - 1 \in [-1,1],$$

the Lagrange polynomials

$$(A.5) \qquad \mathcal{L}_l(\sigma) := \prod_{p=0,p\neq l}^{m} \frac{\sigma - \sigma_p}{\sigma_l - \sigma_p},$$

and the Lagrange interpolant

$$(A.6) \qquad g_{i,j}(\sigma) := \sum_{l=1}^{m+1} y_{i,(m+1)(j-1)+l}\mathcal{L}_l(\sigma),$$

parameterized by its values $y_{i,(m+1)(j-1)+l}$ at the $m+1$ base points $\sigma_1, \ldots, \sigma_{m+1}$.

Given α, there exists a unique integer $j \in \{1, \ldots, N_\alpha\}$ for each value of $t \in (0,T]$ such that

$$(A.7) \qquad \frac{t - t_{\alpha,j}}{T\kappa_{j+1}} \in (-1,1].$$

If we associate $j = 1$ and $\sigma = -1$ with $t = 0$, then the corresponding map

$$(A.8) \qquad \Sigma_\alpha : [0,T] \mapsto \{(j,\sigma) \,|\, 1 \leq j \leq N_\alpha, -1 < \sigma \leq 1, \text{ or } j = 1, \sigma = -1\}$$

is a bijection with inverse given by

$$(A.9) \qquad t = t_{\alpha,j} + \frac{1+\sigma}{2}T\kappa_{\alpha,j+1}.$$

The discretization of the system of differential equations is now complete with the imposition of collocation conditions on the ith equation in terms of a distribution of collocation nodes on the partition π_α. In particular, we choose here to introduce nodes for the jth mesh interval, defined in terms of the local variable σ by the m roots $z_1, \ldots, z_m$ of the mth degree Legendre polynomial on the interval $[-1,1]$. The maps $\{\Sigma_\alpha\}_{\alpha \in \mathcal{A}}$ and their inverses may then be used to identify the associated pairs (j,σ) for each component of y appearing in the ith component of the vector field.

Now let the $1 \times N_\alpha(m+1)$ matrix

$$(A.10) \qquad \mathsf{y}_i := \begin{pmatrix} \cdots & y_{i,(m+1)(j-1)+1} & \cdots & y_{i,(m+1)j} & \cdots \end{pmatrix}$$

collect the base point values for all of the polynomial approximants of y_i, and define the column matrix

$$(A.11) \qquad \mathsf{y}_{bp} = \begin{pmatrix} \mathsf{y}_1 & \cdots & \mathsf{y}_n \end{pmatrix}^T.$$

Continuity across each of the mesh nodes may then be expressed in terms of the linear condition $\mathsf{Q} \cdot \mathsf{y}_{bp} = 0$ for some (very sparse) matrix Q whose nonzero entries equal 1 or -1.

Similarly, the values of the polynomial approximants appearing in the ith component of the vector field, as well as of their derivatives, evaluated on the collocation nodes associated with the corresponding partition may be obtained in terms of the matrix products $\mathsf{W}_i \cdot \mathsf{y}_{bp}$ and $\mathsf{W}'_i \cdot \mathsf{y}_{bp}$ for some mesh-dependent matrices W_i and W'_i. In the special case of a synchronous mesh with $\mathcal{A} = \{\alpha\}$, let

$$\text{(A.12)} \qquad\qquad \mathsf{W} = \mathsf{Id}_{nN_\alpha} \otimes \mathsf{L}$$

and

$$\text{(A.13)} \qquad\qquad \mathsf{W}' = \mathsf{Id}_{nN_\alpha} \otimes \mathsf{L}',$$

where the (p, l)th entries of the $m \times (m + 1)$ matrices L and L' equal $\mathcal{L}_l(z_p)$ and $\mathcal{L}'_l(z_p)$, respectively. It follows that the matrix products $\mathsf{y}_{cn} = \mathsf{W} \cdot \mathsf{y}_{bp}$ and $\mathsf{y}'_{cn} = \mathsf{W}' \cdot \mathsf{y}_{bp}$ collect the values of all the polynomial approximants and their derivatives at the corresponding collocation nodes.

A.2. Adaptivity. In an adapted mesh, the mesh π_α associated with a group of components of y is chosen to equidistribute an estimated total interpolation error across the corresponding mesh intervals. Specifically, for each i, such that y_i is associated with the mesh π_α, consider the piecewise linear function ϕ_i, with $\phi_i(0) = 0$, that interpolates the mth derivative of the piecewise-polynomial approximant of y_i at the midpoint of each mesh interval. The error distribution function θ_α associated with π_α is then defined by

$$\text{(A.14)} \qquad\qquad \theta_\alpha(t) := \int_0^t \max_i \left| \phi'_i(\tau) \right|^{\frac{1}{m+1}} \, d\tau,$$

and the number of mesh intervals is given by

$$\text{(A.15)} \qquad\qquad N_\alpha = \theta_\alpha(T) \left(\frac{\hat{C}}{\mathrm{TOL}} \right)^{\frac{1}{m+1}}$$

for some known constant $\hat{C}$ and desired tolerance TOL [7]. Let $\theta_{\alpha,j} := \theta_\alpha(t_{\alpha,j})$ for $j = 1, \ldots, N_\alpha$ denote the values of the error distribution function on the corresponding mesh nodes. The values of $\kappa_{\alpha,j}$ for $j = 1, \ldots, N_\alpha$ are then chosen to ensure that $\theta_{\alpha,j} - \theta_{\alpha,j-1} = \theta_\alpha(T)/N_\alpha$.

Adaptivity during continuation results in changes to the discretization parameters N_α and $\kappa_{\alpha,j}$ along the collection of computed solutions to the collocation problem. Such changes may result in changes to the embedding dimension of the continuation problem, as well as to the interpretation of individual unknowns. Continuation beyond each such adaptive change is accomplished by sampling a previously obtained piecewise-polynomial solution in order to compute an initial solution guess for the new collection of unknown base point values. Similar interpolation may also be applied to each tangent vector along the original solution manifold in order to estimate the tangent space to the new solution manifold.

The decision to partition the components of y according to a discrete set of meshes may be rationalized in terms of a constrained minimization problem. To this end, suppose that $\mathcal{A} = \{1, \ldots, Q\}$ for some integer $Q \leq n$ and that, without loss of generality, the sequence

$\{\theta_{q,N_q}\}_{q=1}^{Q}$ is increasing. Let z_q denote the number of components of y associated with the mesh π_q such that

$$(A.16) \qquad \sum_{q=1}^{\infty} z_q = n.$$

The total number of mesh intervals is then given by

$$(A.17) \qquad N = \sum_{q=1}^{\infty} z_q N_q = \left(\frac{\hat{C}}{\text{TOL}} \right)^{\frac{1}{m+1}} \sum_{q=1}^{\infty} z_q \theta_{q,N_q}.$$

Let Θ be a smooth, increasing function such that $\Theta(0) = 0$ and

$$(A.18) \qquad \Theta\left(\sum_{r=1}^{q} z_r \right) = \theta_{q,N_q}.$$

It follows that

$$(A.19) \qquad N = N(z_1, \ldots, z_Q) := \left(\frac{\hat{C}}{\text{TOL}} \right)^{\frac{1}{m+1}} \sum_{q=1}^{Q} \left(z_q \Theta\left(\sum_{r=1}^{q} z_r \right) \right).$$

For an *optimal partition*, we now require that the sequence $\{z_q\}_{q=1}^{Q}$ be a solution to the constrained optimization problem

$$(A.20) \qquad \min_{\sum_{q=1}^{Q} x_q = n} N(x_1, \ldots, x_Q).$$

For the corresponding optimization problem on $\mathbb{R}^Q$, for each $i = 1, \ldots, Q$, it follows that

$$(A.21) \qquad \Theta\left(\sum_{r=1}^{i} z_r \right) + \sum_{q=i}^{Q} z_q \Theta'\left(\sum_{r=1}^{q} z_r \right) + \lambda = 0$$

in terms of the Lagrange multiplier λ. Elimination of λ using the equation for $i = Q$ then yields

$$(A.22) \qquad \Theta\left(\sum_{r=1}^{i} z_r \right) + \sum_{q=i}^{Q-1} z_q \Theta'\left(\sum_{r=1}^{q} z_r \right) = \Theta(n)$$

for $i = 1, \ldots, Q-1$. We approximate the derivatives in (A.22) using finite differences to obtain

$$(A.23) \qquad \Theta\left(\sum_{r=1}^{i} z_r \right) + \sum_{q=i}^{Q-1} \left(\Theta\left(\sum_{r=1}^{q} z_r \right) - \Theta\left(\sum_{r=1}^{q-1} z_q \right) \right) = \Theta(n)$$

or, equivalently,

$$(A.24) \qquad \theta_{i,N_i} - \theta_{i-1,N_{i-1}} = \theta_{Q,N_Q} - \theta_{Q-1,N_{Q-1}}$$

for $i = 1, \ldots, Q-1$ and with $\theta_{0,N_0} := 0$. It follows that an optimal partition is one for which the values θ_{i,N_i} for $i = 1, \ldots, Q$ are successive integer multiples of θ_{1,N_1}.

Inspired by this observation, in practice we implement the following algorithm. Let $\hat{\theta}_i$ denote the values of θ_{i,N_i} for a partition in which π_i is associated with the ith component of y, and the components are numbered such that $\hat{\theta}_1, \ldots, \hat{\theta}_n$ is an increasing sequence. Then, for a given integer $Q \le n$, implement an alternative partition in which the ith component of y belongs to the jth partition provided that

$$(A.25) \qquad \frac{\hat{\theta}_n}{Q}(j-1) < \hat{\theta}_i \le \frac{\hat{\theta}_n}{Q}j$$

for $j = 1, \ldots, Q$.

We may judge the closeness of this partition to an optimal choice by the deviation of the corresponding sequence of accumulated errors from the ideal case given in (A.24). In particular, we expect a near-optimal construction when components of y that end up in the same partition exhibit a similar distribution of values of ϕ' on $[0, T]$.

A.3. Performance. We investigate the application of an adaptive asynchronous collocation scheme to the FitzHugh–Nagumo model [21]

$$(A.26) \qquad \dot{v} = c\left(v - \frac{1}{3}v^3 + w\right), \quad \dot{w} = -\frac{v + bw}{c}$$

in order to compare the observed convergence rates in the estimated error with those found using a synchronous mesh with or without adaptation. Specifically, we seek continuous piecewise-polynomial approximants $v(t)$ and $w(t)$ to the periodic solution $(v_{\mathrm{per}}, w_{\mathrm{per}})$ obtained for $b = 0.8$ and $c = 3$ and shown in Figure 16 (computed using a uniform, synchronous mesh with $N = 10^6$).

Here, we examine three different cases, viz., (i) a uniform synchronous mesh, (ii) an adapted synchronous mesh, and (iii) an adapted asynchronous mesh. For each numerical experiment, we report on discretization errors in terms of the supremum norm $\varepsilon_{\mathrm{u}} := \sup_t |v(t) - v_{\mathrm{per}}(t)|$ (in the upper-left and lower-left panels of Figures 17 and 18), and on the maximum norms $\varepsilon_{\mathrm{s}} := \max_i |v(t_{v,i}) - v_{\mathrm{per}}(t_{v,i})|$ (in the upper-right and lower-right panels of Figures 17 and 18). Although not reported in this paper, similar results were obtained for error convergence corresponding to variable w. For each mesh, we let $h = T \max_i \kappa_i$ and estimate the convergence rate r associated with the asymptotic behavior $\mathcal{O}(h^r)$ of each of the discretization errors. In each case, the appropriate mesh selection algorithm is used to generate an initial mesh with $N = 10$ corresponding to the $h_0/h = 1$ rows in each of the tables. Further rows are generated by halving each of the mesh intervals (without any further adaptation).

As a reference, we recall from [39] the theoretical values of $r = m + 1$ and $r = 2m$ for the corresponding convergence rates in case (i). The data in Figure 17 confirms this
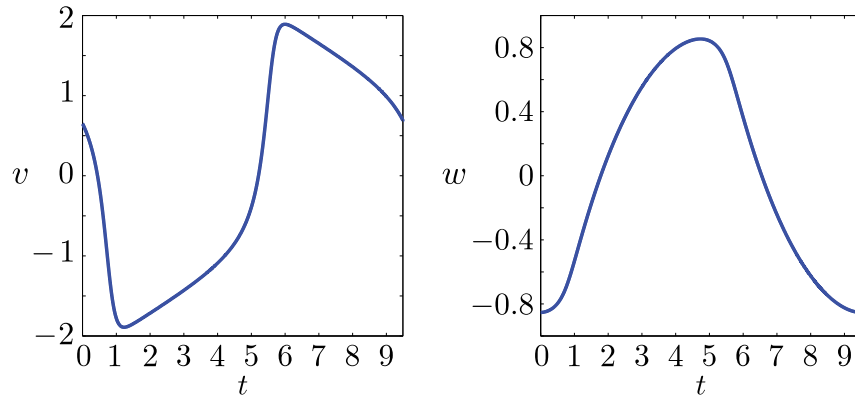
Figure 16. *Periodic solutions of the FitzHugh–Nagumo dynamical system for $b = 0.8$ and $c = 3$.*
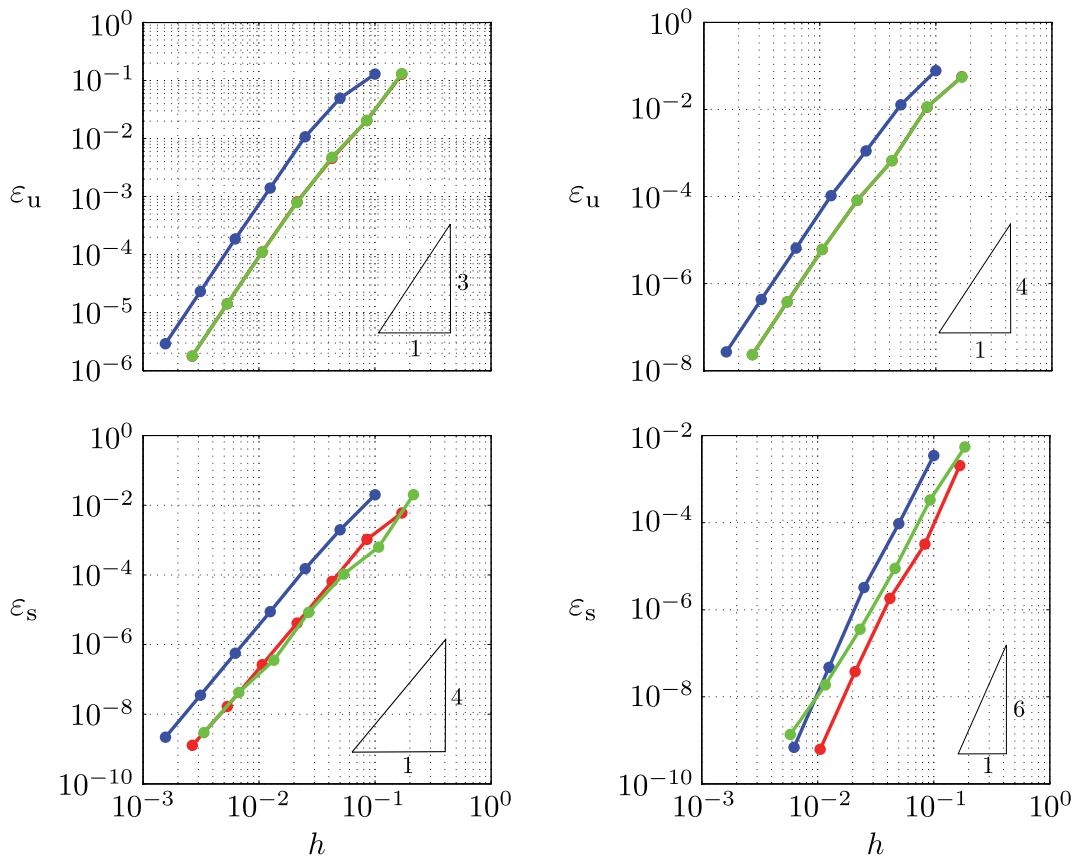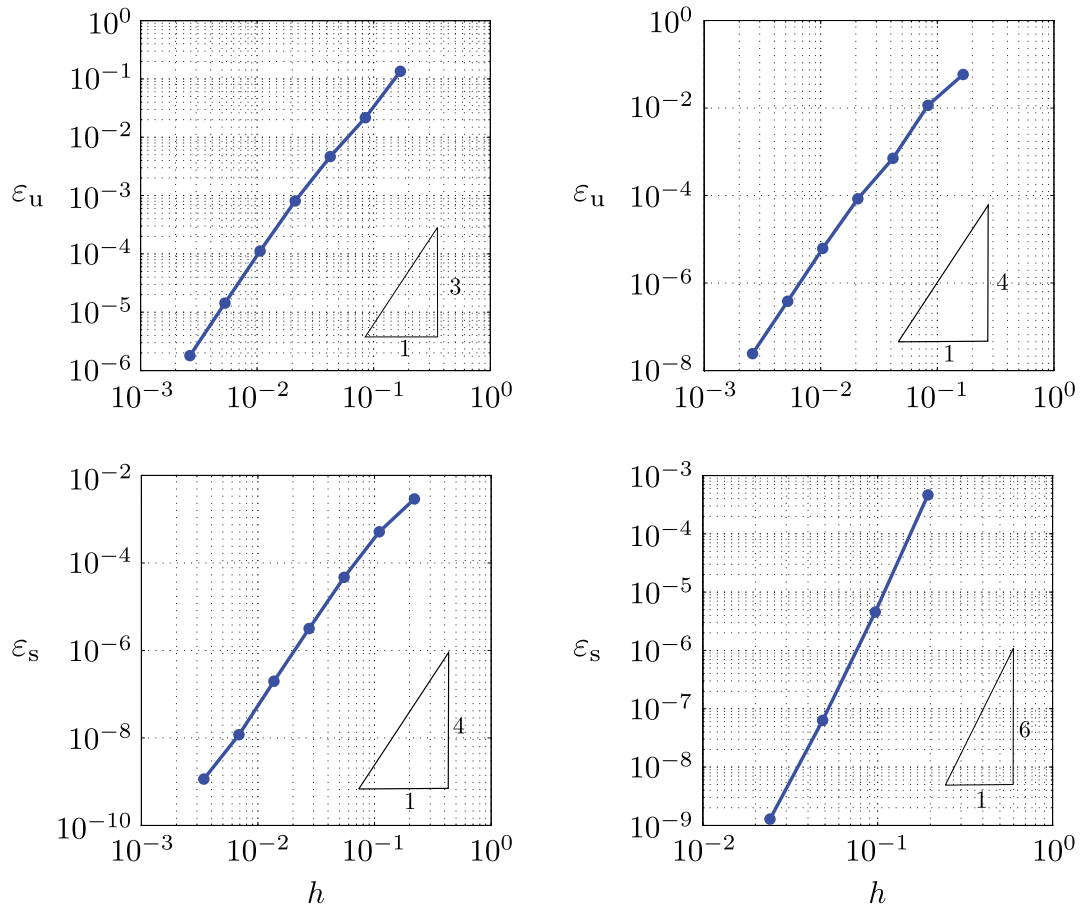

Figure 17. *The upper panels show the convergence of the uniform error for $m = 2$ (left) and $m = 3$ (right). The lower panels show the convergence of the error at the mesh points for $m = 2$ (left) and $m = 3$ (right). Blue, red, and green correspond to cases with uniform synchronous mesh, adapted synchronous mesh, and adapted asynchronous mesh, respectively.*

Figure 18. *The upper panels show the convergence of the uniform error for $m = 2$ (left) and $m = 3$ (right). The lower panels show the convergence of the error at the mesh points for $m = 2$ (left) and $m = 3$ (right).*

theoretical prediction, shows the same rates of convergence in case (ii), and shows a lower rate of convergence in case (iii), especially for the maximal discretization error across the variable-specific mesh nodes. The latter is caused by the interpolation errors within a mesh interval of one variable propagating to the mesh-point errors of the other variable. This coupling of errors is further explored by the data in Figure 18. Here, a fine uniform mesh is used for w in order to ensure that the corresponding interpolation error is of the same order as the mesh-point discretization error associated with the adaptive asynchronous mesh for v. The resulting convergence rates again agree with the theoretical predictions for the synchronous case.

Appendix B. Proof. We comment briefly on the analysis in Pinsky et al. [35] of the differential equation

(B.1) $$\frac{dS}{dh} = 1 - (h - S)^{\frac{1}{3}} S,$$

where h is a monotonically increasing function of time. Here, S again denotes the relative

humidity, and h represents the height of the parcel of air in the atmosphere relative to a reference level. This equation bears some resemblance to (2.36), specifically in the presence of a 1/3 power on the right-hand side. While (2.36) admits the trivial solution $H \equiv 0$, the solution is not unique in forward time. Similarly, it is clear that $S \equiv h$ is a solution to (B.1) with a monotonically increasing variation of S with respect to h. The nondifferentiability of the vector field along this solution, however, implies the possibility of nonuniqueness of solutions and variations in S that achieve a local maximum with respect to h, as found numerically in [35].

Specifically, suppose that at $h = h^*$ we have $S = h^* - \epsilon$, where $0 < \epsilon \ll 1$. We may rearrange (B.1) to obtain

$$\text{(B.2)} \qquad \frac{d(h - S)}{dh} = (h - S(h))^{\frac{1}{3}} S(h).$$

Since $h^* - S(h^*) = \epsilon$ and $S > 0$, we conclude from (B.1) that S is initially increasing with h. Moreover,

$$\left. \frac{d(h - S)}{dh} \right|_{h=h^*} = (h^* - S(h^*))^{\frac{1}{3}} S(h^*)$$

$$\text{(B.3)} \qquad\qquad = h^* \epsilon^{\frac{1}{3}} - \epsilon^{\frac{4}{3}} > 0.$$

This implies, using (B.1), that $\frac{dS}{dh}$ is decreasing. We can further infer from (B.1), (B.2), and (B.3) that both S and $(h - S)$ keep increasing until

$$\text{(B.4)} \qquad (h - S)^{\frac{1}{3}} S = 1,$$

and, hence, a maximum is achieved for S.

As shown by this derivation, arbitrarily small values of ϵ result in a time trajectory that differs qualitatively from the trivial solution obtained for $\epsilon = 0$. We surmise that numerical round-off error (but not truncation error) introduced in the simulations reported in [35] is the reason for finding the nontrivial trajectory, even as the initial conditions correspond to the case that $\epsilon = 0$.

REFERENCES

[1] H. ABDUL-RAZZAK AND S. J. GHAN, *A parameterization of aerosol activation: 2. Multiple aerosol types*, J. Geophys. Res. Atmospheres, 105 (2000), pp. 6837–6844.

[2] H. ABDUL-RAZZAK, S. J. GHAN, AND C. RIVERA-CARPIO, *A parameterization of aerosol activation: 1. Single aerosol type*, J. Geophys. Res. Atmospheres, 103 (1998), pp. 6123–6131.

[3] M. O. ANDREAE, *Correlation between cloud condensation nuclei concentration and aerosol optical thickness in remote and polluted regions*, Atmospher. Chem. Phys., 9 (2009), pp. 543–556.

[4] M. O. ANDREAE AND D. ROSENFELD, *Aerosol-cloud-precipitation interactions. Part 1. The nature and sources of cloud-active aerosols*, Earth-Science Rev., 89 (2008), pp. 13–41.

[5] J. F. ANDRUS, *Numerical solution of systems of ordinary differential equations separated into subsystems*, SIAM J. Numer. Anal., 16 (1979), pp. 605–611.

[6] T. ANTTILA AND V. KERMINEN, *Influence of organic compounds on the cloud droplet activation: A model investigation considering the volatility, water solubility, and surface activity of organic matter*, J. Geophys. Res. Atmospheres, 107 (2002), pp. AAC 12-1–AAC 12-13.

[7] U. M. ASCHER, R. M. MATTHEIJ, AND R. D. RUSSELL, *Numerical Solution of Boundary Value Problems for Ordinary Differential Equations*, Classics Appl. Math. 13, SIAM, Philadelphia, 1988.

[8] T. BELYTSCHKO AND Y. Y. LU, *Convergence and stability analyses of multi-time step algorithm for parabolic systems*, Comput. Methods Appl. Mech. Engrg., 102 (1993), pp. 179–198.

[9] T. BELYTSCHKO AND Y. Y. LU, *Explicit multi-time step integration for first and second order finite element semidiscretizations*, Comput. Methods Appl. Mech. Engrg., 108 (1993), pp. 353–383.

[10] T. BELYTSCHKO, P. SMOLINSKI, AND W. K. LIU, *Stability of multi-time step partitioned integrators for first-order finite element systems*, Comput. Methods Appl. Mech. Engrg., 49 (1985), pp. 281–297.

[11] J. CHING, N. RIEMER, AND M. WEST, *Impacts of black carbon mixing state on black carbon nucleation scavenging: Insights from a particle-resolved model*, J. Geophys. Res. Atmospheres, 117 (2012), D23209.

[12] P. Y. CHUANG, R. J. CHARLSON, AND J. H. SEINFELD, *Kinetic limitations on droplet formation in clouds*, Nature, 390 (1997), pp. 594–596.

[13] U. DUSEK, G. P. FRANK, L. HILDEBRANDT, J. CURTIUS, J. SCHNEIDER, S. WALTER, D. CHAND, F. DREWNICK, S. HINGS, D. JUNG, S. BORRMANN, AND M. O. ANDREAE, *Size matters more than chemistry for cloud-nucleating ability of aerosol particles*, Science, 312 (2006), pp. 1375–1378.

[14] J. M. ESPOSITO AND V. KUMAR, *An asynchronous integration and event detection algorithm for simulating multi-agent hybrid systems*, ACM Trans. Model. Comput. Simul., 14 (2004), pp. 363–388.

[15] C. W. GEAR AND D. R. WELLS, *Multirate linear multistep methods*, BIT, 24 (1984), pp. 484–502.

[16] S. J. GHAN, H. ABDUL-RAZZAK, A. NENES, Y. MING, X. LIU, M. OVCHINNIKOV, B. SHIPWAY, N. MESKHIDZE, J. XU, AND X. SHI, *Droplet nucleation: Physically-based parameterizations and comparative evaluation*, J. Adv. Model. Earth Syst., 3 (2011), M10001.

[17] S. J. GHAN, C. C. CHUNG, AND J. E. PENNER, *A parameterization of cloud droplet nucleation part* I: *Single aerosol type*, Atmospher. Res., 30 (1993), pp. 198–221.

[18] S. J. GHAN, G. GUZMAN, AND H. ABDUL-RAZZAK, *Competition between sea salt and sulfate particles as cloud condensation nuclei*, J. Atmospher. Sci., 55 (1998), pp. 3340–3347.

[19] M. GÜNTHER, A. KVÆRNØ, AND P. RENTROP, *Multirate partitioned Runge-Kutta methods*, BIT, 41 (2001), pp. 504–514.

[20] T. HUGHES, T. BELYTSCHKO, AND W. K. LIU, *Convergence of an element-partitioned subcycling algorithm for the semi-discrete heat equation*, Numer. Methods Partial Differential Equations, 3 (1987), pp. 131–137.

[21] E. M. IZHIKEVICH, *Dynamical Systems in Neuroscience: The Geometry of Excitability and Bursting*, MIT Press, Cambridge, MA, 2006.

[22] N. KIVEKÄS, V. M. KERMINEN, T. ANTTILA, H. KORHONEN, H. LIHAVAINEN, M. KOMPPULA, AND M. KULMALA, *Parameterization of cloud droplet activation using a simplified treatment of the aerosol number size distribution*, J. Geophys. Res. Atmospheres, 113 (2008), D15207.

[23] P. KUMAR, I. N. SOKOLIK, AND A. NENES, *Parameterization of cloud droplet formation for global and regional models: Including adsorption activation from insoluble CCN*, Atmospher. Chem. Phys., 9 (2009), pp. 2517–2532.

[24] A. LEW, J. E. MARSDEN, M. ORTIZ, AND M. WEST, *Asynchronous variational integrators*, Arch. Ration. Mech. Anal., 167 (2003), pp. 85–146.

[25] A. LEW, J. E. MARSDEN, M. ORTIZ, AND M. WEST, *Variational time integrators*, Internat. J. Numer. Methods Engrg., 60 (2004), pp. 153–212.

[26] Y. LIU AND P. H. DAUM, *Anthropogenic aerosols: Indirect warming effect from dispersion forcing*, Nature, 419 (2002), pp. 580–581.

[27] U. LOHMANN AND J. Z. FEICHTER, *Global indirect aerosol effects: A review*, Atmospher. Chem. Phys., 5 (2005), pp. 715–737.

[28] N. MAHOWALD, *Aerosol indirect effect on biogeochemical cycles and climate*, Science, 334 (2011), pp. 794–796.

[29] M. A. MAJEED AND A. S. WEXLER, *Microphysics of aqueous droplets in clouds and fogs as applied to pm-fine modeling*, Atmospher. Environ., 35 (2001), pp. 1639–1653.

[30] Y. MING, V. RAMASWAMY, L. J. DONNER, AND V. T. J. PHILLIPS, *A new parameterization of cloud droplet activation applicable to general circulation models*, J. Atmospher. Sci., 63 (2006), pp. 1348–1356.

[31] A. NENES, S. GHAN, H. ABDUL-RAZZAK, P. Y. CHUANG, AND J. H. SEINFELD, *Kinetic limitations on cloud droplet formation and impact on cloud albedo*, Tellus B, 53 (2001), pp. 133–149.

[32] A. NENES AND J. H. SEINFELD, *Parameterization of cloud droplet formation in global climate models*, J. Geophys. Res. Atmospheres, 108 (2003), 4415.

[33] M. D. PETTERS AND S. M. KREIDENWEIS, *A single parameter representation of hygroscopic growth and cloud condensation nucleus activity*, Atmospher. Chem. Phys., 7 (2007), pp. 1961–1971.

[34] M. PINSKY, A. KHAIN, I. MAZIN, AND A. KOROLEV, *Analytical estimation of droplet concentration at cloud base*, J. Geophys. Res. Atmospheres, 117 (2012), D18211.

[35] M. PINSKY, I. P. MAZIN, A. KOROLEV, AND A. KHAIN, *Supersaturation and diffusional drop growth in liquid clouds*, J. Atmospher. Sci., 70 (2012), pp. 2778–2793.

[36] V. RAMANATHAN, P. J. CRUTZEN, J. T. KIEHL, AND D. ROSENFELD, *Aerosols, climate, and the hydrological cycle*, Science, 294 (2001), pp. 2119–2124.

[37] N. RIEMER, M. WEST, R. ZAVERI, AND R. EASTER, *Estimating black carbon aging time-scales with a particle-resolved aerosol model*, J. Aerosol Sci., 41 (2010), pp. 143–158.

[38] D. ROSENFELD, U. LOHMANN, G. B. RAGA, C. D. O'DOWD, M. KULMALA, S. FUZZI, A. REISSELL, AND M. O. ANDREAE, *Flood or drought: How do aerosols affect precipitation?*, Science, 321 (2008), pp. 1309–1313.

[39] R. D. RUSSELL, *Collocation for systems of boundary value problems*, Numer. Math., 23 (1974), pp. 119–133.

[40] V. SAVCENCO, W. HUNDSDORFER, AND J. G. VERWER, *A multirate time stepping strategy for stiff ordinary differential equations*, BIT, 47 (2007), pp. 137–155.

[41] J. H. SEINFELD AND S. N. PANDIS, *Atmospheric Chemistry and Physics: From Air Pollution to Climate Change*, 2nd ed., John Wiley & Sons, New York, 2006.